

Variational autoencoder for inference of nonlinear mixed effect models based on ordinary differential equations

Zhe Li, Mélanie Prague, Rodolphe Thiébaut, Quentin Clairon *

University of Bordeaux, Department of Public Health,
Inserm Bordeaux Population Health Research Centre, Inria SISTM team,
VRI, France

January 22, 2026

Abstract

We propose a variational autoencoder (VAE) approach for parameter estimation in nonlinear mixed-effects models based on ordinary differential equations (NLME-ODEs) using longitudinal data from multiple subjects. In moderate dimensions, likelihood-based inference via the stochastic approximation EM algorithm (SAEM) is widely used, but it relies on Markov Chain Monte-Carlo (MCMC) to approximate subject-specific posteriors. As model complexity increases or observations per subject are sparse and irregular, performance often deteriorates due to a complex, multimodal likelihood surface which may lead to MCMC convergence difficulties. We instead estimate parameters by maximizing the evidence lower bound (ELBO), a regularized surrogate for the marginal likelihood. A VAE with a shared encoder amortizes inference of subject-specific random effects by avoiding per-subject optimization and the use of MCMC. Beyond pointwise estimation, we quantify parameter uncertainty using observed-information-based variance estimator and verify that practical identifiability of the model parameters is not compromised by nuisance parameters introduced in the encoder. We evaluate the method in three simulation case studies (pharmacokinetics, humoral response to vaccination, and TGF- β activation dynamics in asthmatic airways) and on a real-world antibody kinetics dataset, comparing against SAEM baselines.

Keywords: Variational Bayesian inference; Longitudinal population data analysis; Neural Networks

*The authors gratefully acknowledge Inserm to the booster program *Exposome and SOLVE* funded by the European Union's Horizon Europe Research and Innovation programme under grant N°101137185

1 Introduction

Ordinary differential equation (ODE) models are widely used in systems biology, mathematical medicine, virology, vaccinology, and pharmacometrics due to their interpretability and predictive power. However, classical ODEs typically describe an average trajectory and do not capture inter-individual variability in longitudinal population data, which are often sparse, irregularly sampled, and noisy. To address this, ODEs are commonly embedded in nonlinear mixed-effects (NLME) models, yielding NLME-ODEs ([Lavielle 2014](#)), where subject-specific random effects capture heterogeneity while preserving a shared mechanistic structure.

More formally, NLME-ODEs consider a population of n subjects. For subject $i \in \{1, \dots, n\}$, observations are collected at (possibly irregular) times t_{ij} , $j = 1, \dots, n_i$, where n_i denotes the number of measurements for subject i ; we write Y_{ij} for the measurement taken at time t_{ij} . The dynamics of the subject i is described by a D_X -dimensional ODEs:

$$\begin{cases} \dot{X}_i(t) = f_{\theta_i}(t, X_i(t)), \\ X_i(0) = x_{i,0}, \end{cases}$$

where f_{θ_i} is a D_X -dimensional vector field defining the system dynamics, θ_i is a vector of subject-specific parameters, and $x_{i,0}$ denotes the initial condition. Inter-individual variability is modeled through a mixed-effects formulation $\theta_i = g(\theta, b_i)$, where θ represents the population-level mean and b_i denotes the subject-specific deviation around this mean, also known as the random effects. Here, $g(\cdot)$ is a (possibly nonlinear) transformation function that maps the population parameters θ and the subject-specific random effects b_i to the individual parameter vector θ_i , for example through additive or log-normal parameterizations to enforce constraints such as positivity. We assume $b_i \sim p_\phi(b_i) = \mathcal{N}(0, \Omega)$, where $b_i = (b_{i1}, \dots, b_{id_b})^\top \in \mathbb{R}^{D_b}$ is the D_b -dimensional vector of random effects and $\Omega = \text{diag}(\omega_1^2, \dots, \omega_{d_b}^2)$ is a diagonal covariance matrix, where ω_{d_b} denotes the standard

deviation of the d_b -th random effect ($d = 1, \dots, D_b$).

Our goal is to estimate the population parameters $\phi = (\theta, \Omega, \Sigma)$ of dimension d_ϕ from the noisy and discrete observations Y_{ij} generated according to the following measurement model:

$$Y_{ij} = h_{\theta_i}(X_i(t_{ij})) + \epsilon_{ij}, \quad \epsilon_{ij} \sim \mathcal{N}(\mathbf{0}, \Sigma). \quad (1)$$

Here, $\Sigma = \text{diag}(\sigma_1^2, \sigma_2^2, \dots)$ is the diagonal variance matrix of the measurement noise, h_{θ_i} is the observation function mapping the i -th subject state represented by the ODEs solution X_i to the measure Y_{ij} made at time t_{ij} .

As in classical inference problems, NLME-ODE parameters can be estimated by maximum likelihood, marginalizing over the random effects b_i viewed as latent variables. However, maximizing the marginal likelihood requires repeated integration over b_i , which is generally intractable in nonlinear ODE models. Early approaches such as first-order (FO) and first-order conditional estimation (FOCE) rely on local Taylor/Laplace approximations to obtain a tractable likelihood (Pinheiro & Bates 1994). These approximations can be inaccurate under strong nonlinearities, non-Gaussian random effects, or sparse individual data, settings common in NLME-ODEs; adaptive Gaussian quadrature can improve accuracy (Pinheiro & Bates 2000, Prague et al. 2013) but becomes computationally prohibitive as the number of random effects grows. A widely used method is the stochastic approximation EM (SAEM) algorithm (Delyon et al. 1999, Lavielle & Mentré 2007), which avoids explicit numerical integration by sampling random effects from their conditional distribution (typically via MCMC) and updating parameters through stochastic approximation. SAEM is often more accurate and stable than FO/FOCE or quadrature for nonlinear models and is implemented in Lixoft-SAS (2025), Pumas-AI (2025). Nonetheless, for sparse data and/or high-dimensional random effects, SAEM may become computationally expensive and less reliable, motivating scalable variational alternatives.

SAEM inherits several limitations from its reliance on MCMC in the E-step. In sparse settings, the conditional posterior of the random effects is weakly informed by the data, which can lead to slow mixing and poor exploration. As the dimension of the random effects increases, MCMC becomes increasingly expensive and more sensitive to multimodality, potentially converging to local modes and yielding non-identifiable solutions. Bayesian MCMC-based inference or MAP estimation faces similar computational and convergence issues in the same regimes (Lunn et al. 2000, Carpenter et al. 2017).

More fundamentally, NLME-ODE likelihoods are often highly non-convex because ODE solutions depend nonlinearly on the parameters, producing rugged objective landscapes and compounding identifiability and optimization difficulties. These challenges motivate optimization-based alternatives that can regularize inference and scale to complex models. Variational inference (VI) replaces stochastic sampling with a tractable, parametric approximation of the posterior, optimized by maximizing a lower bound. In particular, variational autoencoders (VAEs) use neural networks to parameterize this approximation, offering a scalable and flexible framework for NLME-ODE inference.

This coupling between NLME-ODEs and neural networks have already been investigated for other purposes. Qian et al. (2021) proposed to integrates expert pharmacological ODEs into Neural ODEs to provide additional insights to the clinicians in disease-progression modeling. Bräm et al. (2025) introduced low-dimensional neural ODEs implemented directly in Lixoft-SAS (2025), showing how inter-individual variability can be incorporated into neural ODEs parameters while preserving pharmacometric interpretability. Janssen et al. (2024) compared FO/FOCE and VI approaches for mixed-effect estimation in Deep Compartment Models. Arruda et al. (2024) developed an amortized inference framework in which a conditional normalizing flow is trained on simulated data generated from the parametric ODE model to approximate the parameter posterior distribution. Martensen et al. (2024) introduced a

Deep Nonlinear Mixed-Effect (Deep-NLME) ([PumasAI 2025](#)) modeling framework in which a neural network term is embedded directly into the ODE to represent unknown system dynamics. [Roeder et al. \(2019\)](#) performed amortised Bayesian inference for NLME-ODEs through a conditional VAE with population-, group-, and individual-level latent blocks.

Despite these advances, most deep or variational extensions of NLME-ODEs emphasize predictive performance and scalability over statistical interpretability and identifiability. Variational/amortized approaches ([Roeder et al. 2019](#), [Arruda et al. 2024](#)) provide efficient posterior approximations but do not explicitly address identifiability or uncertainty calibration in parametric ODE settings. Conversely, methods that embed neural networks into pharmacometric ODEs ([Bräm et al. 2025](#), [Martensen et al. 2024](#)) typically rely on SAEM or FOCE, and thus remain computationally demanding, and sensitive to initialization; moreover, neural components is generally nonidentifiable due to redundancy. Even VAE based inference methods for NLME-ODE close to our methodology have been recently proposed in [Rohleff et al. \(2025\)](#), they undermine the issues of practical identifiability and uncertainty quantification, by ignoring the construction of a variance estimator, on which we focus here since these points are crucial to ensure the interpretability of the obtained estimator. In particular, they do not proceed to rigorous comparison with SAEM based methods on these matter.

In this paper, we propose a amortized variational inference framework for NLME-ODEs tailored to sparse and irregular longitudinal settings, while preserving mechanistic interpretability and identifiability. We maximize the evidence lower bound (ELBO), yielding a tractable objective that avoids the sampling step of SAEM. For each subject, the posterior distribution of random effects is approximated within a parametric family parameterized by a lightweight, shallow neural encoder to prevent overfitting and non-identifiability given the limited data; the decoder is a parametric ODE model which reconstructs the trajectory

from the random effects, ensuring that the inferred representations retain a mechanistic interpretation as subject-specific biological parameters. Although the method is compatible with higher-dimensional random-effects structures, in this work we primarily evaluate its performance in data-scarce regimes and leave a systematic study of scalability with respect to the random-effect dimension to future work.

Beyond point estimation, we quantify population-level parameter uncertainty via a variance estimator based on the observed Fisher information matrix, computed by automatic differentiation at the variational optimum for population parameters.

Identifiability is fundamental for interpretable inference in NLME models. When neural network components are introduced, this property can be compromised by additional nuisance parameters or redundant representations. We further assess convergence behavior to verify the practical identifiability of the underlying ODEs, ensuring that each population parameter can be uniquely determined from the data. These steps guarantee that the resulting inference remains stable and interpretable within the NLME-ODEs framework.

The paper is organized as follows: **Section 2** introduces the proposed method, including the variational inference strategy, identifiability analysis, and uncertainty quantification procedure; **Section 3** reports simulation results in which we compare our method with the approach SAEM implemented in Monolix ([Lixoft-SAS \(2025\)](#)) in terms of estimation accuracy and identifiability issues under various scenarios, in particular for the estimation of NLME-ODEs of increasing complexities in terms of numbers of estimated parameters; **Section 4** presents an application to real clinical data on antibody concentration dynamics following immunization with a COVID-19 vaccine ([Clairon et al. 2023](#)), demonstrating the practical relevance and robustness of the proposed framework.

2 Amortized Variational Inference for NLME–ODEs

2.1 Marginal Likelihood and Variational Reformulation

Classical inference methods for NLME models are based on maximizing the marginal log likelihood over the population, given by:

$$\ell(\phi; \mathbf{Y}) = \sum_{i=1}^n \log p_\phi(Y_i), \quad (2)$$

where

$$\log p_\phi(Y_i) = \log \int p_\phi(Y_i \mid b_i) p_\phi(b_i) db_i, \quad (3)$$

$$= \log \int \left[\prod_{j=1}^{n_i} \mathcal{N}(Y_{ij} - h_{\theta_i}(X_i(t_{ij})), \Sigma) \right] p_\phi(b_i) db_i. \quad (4)$$

is the individual log likelihood. $\mathbf{Y} = \{Y_1, \dots, Y_n\}$ represents the aggregated data for the n subjects in the population where $Y_i = \{Y_{ij}\}_{j=1..n_i}$ is the vector of observations for the i -th subject measured at the n_i timepoints $\{t_{ij}\}_{j=1, \dots, n_i}$. Here, $\mathcal{N}(Y_{ij} - h_{\theta_i}(X_i(t_{ij})), \Sigma)$ denotes the density of a centered Gaussian distribution with covariance matrix Σ , evaluated at the residual $Y_{ij} - h_{\theta_i}(X_i(t_{ij}))$, as implied by the observation model (1). The integral over b_i is analytically intractable in many nonlinear settings. Instead of relying on approximate numerical integration or MCMC, we adopt a variational inference approach. We introduce a variational distribution $q_\psi(b_i \mid Y_i) = \mathcal{N}(\mu_\psi(Y_i), \Sigma_\psi(Y_i)^\top)$, where $\mu_\psi(Y_i)$ is the variational mean and $\Sigma_\psi(Y_i)$ is a diagonal standard-deviation matrix. This distribution approximates the intractable posterior $p_\phi(b_i \mid Y_i)$ from which the individual evidence lower bound (ELBO) is derived (Kingma & Welling 2014):

$$\mathcal{L}_{\text{elbo}_i}(\phi, \psi; Y_i) = \underbrace{\mathbb{E}_{q_\psi(b_i \mid Y_i)} [\log p_\phi(Y_i \mid b_i)]}_{\text{data fidelity}} - \underbrace{\text{KL}(q_\psi(b_i \mid Y_i) \parallel p_\phi(b_i))}_{\text{regularization}}. \quad (5)$$

thus the training objective function for the population is:

$$\mathcal{L}_{\text{ELBO}}(\phi, \psi; \mathbf{Y}) = \sum_{i=1}^n \mathcal{L}_{\text{elbo}_i}(\phi, \psi; Y_i) \quad (6)$$

which satisfies $\ell(\phi; \mathbf{Y}) \geq \mathcal{L}_{\text{ELBO}}(\phi, \psi; \mathbf{Y})$ by Jensen's inequality, more details about the ELBO derivation are recalled in Appendix Section 1. In our model, we have two distinct sets of parameters:

1. structural parameter of interest: the vector field parameter, the standard deviation of random effects and measurement noise: $\phi = (\theta, \Omega, \Sigma)$ with the dimension denoted as D_ϕ .
2. nuisance parameters: the parameter ψ with the dimension denoted as D_ψ required for a posteriori approximator q_ψ .

So the estimator can be defined as:

$$(\hat{\phi}, \hat{\psi}) = \arg \max_{(\phi, \psi)} \mathcal{L}_{\text{ELBO}}(\phi, \psi; \mathbf{Y}) \quad (7)$$

2.2 Variational Autoencoder

To optimize the ELBO, we adopt amortized variational inference (Kingma & Welling 2014), where a shared neural network encoder parameterized by ψ maps each subject's longitudinal observations to the parameters of the approximate posterior. The expressiveness of the variational family can be adapted to data availability and model complexity. In this work we use a Gaussian family for computational efficiency, but richer distributions (e.g., Gaussian mixtures or normalizing flows) can be employed when greater flexibility is required. The encoder outputs $\mu_\psi(Y_i)$ and $\Sigma_\psi(Y_i)$ of the approximate posterior distribution. Coupled with an ODEs-based decoder that reconstructs the data from the random effects, this architecture forms a VAE adapted to NLME-ODEs.

Amortized inference offers several advantages in the context of longitudinal data with sparse available measurement per subject, such as in clinical trial setting. By sharing statistical strength across subjects, it improves inference stability even when individual trajectories

are short, sparse, or irregularly sampled. Once trained, the encoder provides near-instant posterior estimates for new subjects, making the approach computationally efficient and scalable to large cohorts. Furthermore, by learning a smooth mapping from observed data to latent parameters, the amortized encoder regularizes the inverse problem, reducing overfitting and enhancing generalization to unseen clinical profiles.

The encoder architecture depends on the sampling design of the longitudinal data. For regularly sampled trajectories with fixed sequence length, we use a lightweight encoder combining one-dimensional convolutional and projection layers with smooth nonlinear activation functions such as the Gaussian Error Linear Unit (GELU). Given the regular grid, local temporal dependencies can be captured effectively by convolutions, and compared with recurrent architectures, this design uses fewer parameters and is therefore less prone to overfitting in our setting, while maintaining numerical stability and identifiability of the model parameters. For irregularly sampled trajectories, we instead use a recurrent encoder, which takes as input both the observed values and the elapsed time between successive measurements ($\Delta t_{ij} = t_{ij} - t_{i,j-1}$), together with a normalized absolute time covariate. These additional time inputs allow the network to adapt its dynamics to heterogeneous sampling intervals, which is crucial when the timing of observations carries information about the underlying process. Given the limited size of the data in our application, we use shallow architectures with small hidden dimensions smaller than 32 to limit overfitting and avoid introducing non-identifiability due to excessive network capacity.

In real-world applications, longitudinal sequences typically have variable lengths. To enable efficient batching, we pad each sequence to a common length T (the maximum sequence length in the dataset) and define a binary mask $m_{it} \in \{0, 1\}$ indicating whether time step t for subject i is observed ($m_{it} = 1$) or corresponds to padding/missingness ($m_{it} = 0$). The masked attention pooling is applied by aggregating variable-length sequences into a

fixed-dimensional subject representation throughout the encoder. In the reconstruction term, the mask ensures that padded positions does not contribute to the objective (Vaswani et al. 2017).

Given a latent sample b_i , the decoder reconstructs the corresponding subject-specific dynamics by integrating the nonlinear ODEs system $X_i(t) = \text{ODESolve}(f_{\theta_i}, x_{i,0}, t)$. We solve the mechanistic ODE systems using adaptive time-stepping methods, selecting the solver according to the stiffness properties of the dynamics. For non-stiff or mildly stiff systems, we use an explicit Runge–Kutta method of order five. For models exhibiting moderate stiffness, we use a fifth-order diagonally implicit Runge–Kutta scheme, which provides improved stability in the presence of fast transient modes. Relative and absolute error tolerances are set adaptively and specified per model in the corresponding experimental section. All integrations are performed with the `Diffra`x library (Kidger 2022).

During the training, the parameters are updated using Adam (Kingma & Ba 2015), with gradients computed via automatic differentiation in `Optax` (Google DeepMind 2020). More details of the optimization, in particular the stopping criterion rules, are in the Appendix Section 4.

2.2.1 Pitfall of posterior collapse

A well-known failure mode in VAE is posterior collapse (Wang et al. 2021, Dai et al. 2020), where the encoder learns a distribution too close to the prior which is fixed as $\mathcal{N}(\mathbf{0}, I_{D_b})$ and fails to capture individual-level variability. In our case, the risk of posterior collapse is inherently reduced due to two modeling choices:

- Learned variance of the prior Ω : Instead of fixing the prior, we jointly learn its covariance structure, which increases flexibility and prevents the prior from dominating the variational posterior;

- ODEs decoder conditioned on b_i : The subject-specific random effects b_i directly influences the ODEs vector field, ensuring it has a non-negligible effect on the data likelihood.

2.3 Parameters Identifiability Analysis

Parameter identifiability is a fundamental requirement in mixed-effects and dynamical system modeling, as it determines whether model parameters can be uniquely inferred from observed data. In the context of inverse problems, accurate and interpretable parameter estimation depends critically on this property: a model is identifiable if distinct parameter values yield distinct distributions of the data. Formally, identifiability is defined as

$$\forall \phi_1, \phi_2 \in \Phi, \quad p_{\phi_1}(\mathbf{Y}) = p_{\phi_2}(\mathbf{Y}) \Rightarrow \phi_1 = \phi_2.$$

This ensures that the mapping from parameters ϕ to the data distribution $p_\phi(\mathbf{Y})$ is injective.

We distinguish structural identifiability, which concerns the uniqueness of parameters given perfect, noise-free observations of the system's states (Bellman & Åström 1970, Audoly et al. 2001), from practical identifiability, which reflects the ability to recover parameters from finite and noisy data (Raue et al. 2009, Lavielle & Aarons 2016).

In this work, we assume that the structural identifiability of the ODEs is established, that is, the underlying biological dynamics are parameterized in a way that allows unique recovery of the true parameters under ideal conditions. We assess practical identifiability empirically by repeatedly reinitializing the estimation procedure from different random parameter values, also called convergence assessment. Consistent convergence of the learned parameters across runs suggests practical identifiability and indicates that the inference algorithm avoids the local optima that often arise in classical likelihood-based methods and signal non-identifiability.

2.4 Uncertainty Quantification of Population-Level Parameters

By assuming that the approximate variational posterior $q_{\hat{\psi}}(b_i|Y_i)$ provides a sufficiently accurate approximation of the true posterior p_{ϕ} , we estimate the variance of $\hat{\phi}$ using the inverse observed Fisher information derived from the marginal likelihood.

Following Margossian & Blei (2024), the individual ELBO error decomposes as:

$$\log p_{\phi}(Y_i) - \mathcal{L}_{\text{elbo},i}(\phi, \psi; Y_i) = \underbrace{\left[\log p_{\phi}(Y_i) - \mathcal{L}(\phi, q^*; Y_i) \right]}_{\text{variational gap}} + \underbrace{\left[\mathcal{L}(\phi, q^*; Y_i) - \mathcal{L}_{\text{elbo},i}(\phi, \psi; Y_i) \right]}_{\text{amortization gap}},$$

where $q^*(b_i | Y_i) \in \mathcal{Q}$ maximizes the ELBO in the chosen variational family. The amortization gap arises because a single encoder $q_{\psi}(b_i | Y_i)$ amortizes inference across subjects rather than optimizing a separate q_i for each subject i . Margossian & Blei (2024) show that this gap can vanish when an ideal inference function exists and the encoder class is sufficiently expressive for exchangeable latent-variable models with $p_{\phi}(b, \mathbf{Y}) = \prod_{i=1}^n p_{\phi}(b_i) p_{\phi}(Y_i | b_i)$. Our NLME-ODE model satisfies this factorization since $b_i \sim \mathcal{N}(\mathbf{0}, \Omega)$ are i.i.d. given ϕ . Hence an ideal mapping $f^*(Y_i)$ to the optimal variational parameters exists, and when $q_{\psi}(b_i | Y_i)$ approximates f^* within the Gaussian family, the amortization gap is negligible.

The variational gap equals $\text{KL}(q^*(b_i | Y_i) \| p_{\phi}(b_i | Y_i))$ and generally does not vanish for a fixed \mathcal{Q} due to variational misspecification. In our framework, we do not place a prior distribution on the population parameters ϕ ; instead, (ϕ, ψ) are learned by maximizing the population-level ELBO: $(\hat{\phi}, \hat{\psi}) = \arg \max_{\phi, \psi} \frac{1}{n} \sum_{i=1}^n \mathcal{L}_{\text{elbo},i}(\phi, \psi; Y_i)$, so $(\hat{\phi}, \hat{\psi})$ is an M-estimator with ψ a shared nuisance parameter. Equivalently, $\hat{\phi}$ maximizes the profiled criterion $M_n(\phi) = \frac{1}{n} \sum_{i=1}^n \mathcal{L}_{\text{elbo},i}(\phi, \hat{\psi}; Y_i)$. If the variational gap (and its ϕ -derivatives) is uniformly small near the true parameter, maximizing the ELBO is close to maximizing $\frac{1}{n} \sum_{i=1}^n \log p_{\phi}(Y_i)$, so that $\hat{\phi}$ behaves like a quasi-MLE.

When both gaps are small, the population ELBO tightly approximates the marginal log-likelihood. In this regime, we quantify uncertainty in $\hat{\phi}$ by approximating $\log p_{\phi}(Y_i)$ via

Monte Carlo over b_i and computing the Hessian at $\hat{\phi}$, yielding the observed information

$$I_n(\hat{\phi}) = - \sum_{i=1}^n \nabla_{\phi}^2 \log p_{\hat{\phi}}(Y_i), \quad (8)$$

where $p_{\hat{\phi}}(Y_i)$ denotes the marginal likelihood for subject i at $\hat{\phi}$.

To evaluate $p_{\hat{\phi}}(Y_i)$ and its derivatives, we apply a Monte Carlo approximation based on the reparameterization trick. We express the random effects b_i as a transformation of a noise variable $p_{\epsilon} \sim \mathcal{N}(\mathbf{0}, I_{D_b})$ independent of ϕ : $b_i = \mathcal{T}_{\hat{\phi}}(\epsilon) = \hat{\Omega}^{1/2}\epsilon$ where $\hat{\Omega}^{1/2}$ is the estimated standard deviation matrix of the prior distribution $p_{\hat{\phi}}(b_i)$ which is assumed to be a zero-mean Gaussian. So we can approximate the marginal likelihood using monte carlo as:

$$p_{\hat{\phi}}(Y_i) \approx \frac{1}{L} \sum_{\ell=1}^L p_{\hat{\phi}}\left(Y_i \mid b_i^{(\ell)}\right) = \frac{1}{L} \sum_{\ell=1}^L p_{\hat{\phi}}\left(Y_i \mid \mathcal{T}_{\hat{\phi}}(\epsilon^{(\ell)})\right), \quad p_{\epsilon^{(\ell)}} \sim \mathcal{N}(\mathbf{0}, I_{D_b}). \quad (9)$$

The corresponding gradient and Hessian of the marginal likelihood are:

$$\begin{aligned} \nabla_{\phi} p_{\hat{\phi}}(Y_i) &= \mathbb{E}_{p(\epsilon)}\left[\nabla_{\phi} p_{\hat{\phi}}(Y_i \mid \mathcal{T}_{\hat{\phi}}(\epsilon))\right] \approx \frac{1}{L} \sum_{\ell=1}^L \nabla_{\phi} p_{\hat{\phi}}(Y_i \mid \mathcal{T}_{\hat{\phi}}(\epsilon^{(\ell)})), \\ \nabla_{\phi}^2 p_{\hat{\phi}}(Y_i) &= \mathbb{E}_{p(\epsilon)}\left[\nabla_{\phi}^2 p_{\hat{\phi}}(Y_i \mid \mathcal{T}_{\hat{\phi}}(\epsilon))\right] \approx \frac{1}{L} \sum_{\ell=1}^L \nabla_{\phi}^2 p_{\hat{\phi}}(Y_i \mid \mathcal{T}_{\hat{\phi}}(\epsilon^{(\ell)})). \end{aligned}$$

Finally, The Hessian of the log-marginal likelihood is computed as:

$$\nabla_{\phi}^2 \log p_{\hat{\phi}}(Y_i) = \frac{\nabla_{\phi}^2 p_{\hat{\phi}}(Y_i) \cdot p_{\hat{\phi}}(Y_i) - \nabla_{\phi} p_{\hat{\phi}}(Y_i) \nabla_{\phi} p_{\hat{\phi}}(Y_i)^{\top}}{p_{\hat{\phi}}(Y_i)^2}. \quad (10)$$

2.5 Subject-specific parameter estimators

In NLME models, after estimating the population parameters, likelihood-based methods provide subject-specific parameter estimates known as Empirical Bayes estimates, defined as the maximizers of the estimated a posteriori distributions $\hat{b}_i^{\text{EBE}} = \arg \max_{b_i} p_{\hat{\phi}}(b_i \mid Y_i) \propto p_{\hat{\phi}}(Y_i \mid b_i) p_{\hat{\phi}}(b_i)$, where $\hat{\phi}$ denote the estimated population parameters. In our framework, once trained, $q_{\hat{\phi}}(b_i \mid Y_i)$ is an approximation of $p_{\hat{\phi}}(b_i \mid Y_i)$ from which we can approximate the Empirical bayes estimates. Since, by construction, $q_{\hat{\phi}}(b_i \mid Y_i)$ is Gaussian with mean

$\mu_\psi(Y_i)$ and standard deviation $\Sigma_\psi(Y_i)$, we obtain $\hat{b}_i^{\text{EBE}} = \arg \max_{b_i} q_{\hat{\psi}}(b_i \mid Y_i) = \mu_{\hat{\psi}}(Y_i)$.

This interpretation bridges variational inference and the classical Empirical Bayes estimation step, enabling scalable inference of individual effects in high-dimensional NLME-ODEs.

3 Simulations

To validate our approach, we evaluate its performance and compare it with a classic likelihood/SAEM based approach on several benchmarks constituted of synthetic data simulated from NLME-ODEs with known ground-truth parameters. We assess the accuracy of pointwise estimation via a Monte-Carlo approach in which $N_{\text{MC}} = 100$ trials of simulated data are constituted from which parameters are estimated. While larger Monte Carlo sample sizes (e.g., $N_{\text{MC}} = 1000$) are often recommended, we found $N_{\text{MC}} = 100$ to provide stable estimates given the substantial computational cost of each fit. From the estimated parameters $\hat{\phi}_{\text{VAE}_k}$ and $\hat{\phi}_{\text{LL}_k}$ where $k = 1, \dots, N_{\text{MC}}$ obtained from our approach and Monolix (based on SAEM) respectively, we compare pointwise estimation accuracy using three standard metrics:

- Relative Root Mean Squared Error: $\text{RRMSE} = \frac{1}{\phi} \sqrt{\frac{1}{N_{\text{MC}}} \sum_{k=1}^{N_{\text{MC}}} (\hat{\phi}_k - \phi)^2}$;
- Relative Bias: $\text{Rel.Bias} = \frac{1}{\phi} \left(\frac{1}{N_{\text{MC}}} \sum_{k=1}^{N_{\text{MC}}} \hat{\phi}_k - \phi \right)$;
- Empirical Variance: $\text{Emp.Var.} = \frac{1}{N_{\text{MC}}} \sum_{k=1}^{N_{\text{MC}}} \hat{\phi}_k^2 - \left(\frac{1}{N_{\text{MC}}} \sum_{k=1}^{N_{\text{MC}}} \hat{\phi}_k \right)^2$.

We compute the estimated variance (Est. Var) for our approach described in section 2.4 for each obtained $\hat{\phi}_{\text{VAE}_k}$ and the classic Fisher based one available for $\hat{\phi}_{\text{LL}_k}$. The accuracy of the variance estimation is then assessed by comparison of the theoretical variance approximated this way with the empirical one described before which are supposed to estimate the same quantity. We also evaluate the frequentist coverage rate of the 95% confidence interval derived from the Est. Var and Emp. Var (Est. Cov and Emp. Cov). We systematically

evaluate practical identifiability for each inference procedure.

All experiments were run on a single machine equipped with an NVIDIA A100 GPU (40 GB), using float64 precision. Importantly, the proposed VAE-based NLME-ODE approach is not GPU-intensive: we were able to run the full pipeline on a standard laptop (Intel Core i7 CPU with an NVIDIA RTX 2000 GPU) including the variance estimation step, though it is slower than on the A100. For the SAEM benchmark, we used `Monolix 2023R1` on a high-performance CPU server equipped with 2x 16-core Skylake Intel Xeon Gold 6142 @ 2.6 GHz and 384 GB of RAM. The implementation details are in the Appendix Section 5.

3.1 Pharmacokinetic

3.1.1 Simulation setting

To assess the accuracy and robustness of our variational inference framework, we start the comparison with a classic and partially observed pharmacokinetic model with first-order absorption and elimination rates defined by the following subject-specific ODEs:

$$\begin{cases} \dot{X}_{1,i}(t) = \vartheta_2 X_{2,i}(t) - \vartheta_{1,i} X_{1,i}(t), \\ \dot{X}_{2,i}(t) = -\vartheta_2 X_{2,i}(t), \\ (X_{1,i}(0), X_{2,i}(0)) = (2, 3), \end{cases} \quad (11)$$

where $\vartheta_{1,i}, \vartheta_2$ are the parameters governing the decay and transfer rates between two compartments. Structural identifiability of the system in Eq. (11) holds provided that the initial conditions are known and at least one state variable (typically $X_{1,i}$) is observed continuously over time.

The parameter $\vartheta_{1,i}$ varies across individuals and is modeled as:

$$\log(\vartheta_{1,i}) = \log(\vartheta) + b_i, \quad b_i \sim \mathcal{N}(0, \omega_{\vartheta_1}^2),$$

where ϑ_1 is the population-level mean and ω_{ϑ_1} is the standard deviation of the random effect. The dataset consists of 100 subjects. For each subject i , we observe 6 noisy partial observations of the first state $X_{1,i}$ at time points t_{ij} over the interval $T = [0, 10]$:

$$Y_{ij} = X_{1,i}(t_{ij}) + \epsilon_{ij}, \quad \epsilon_{ij} \sim \mathcal{N}(0, \sigma_\epsilon^2),$$

as illustrated in Figure 2(a). The true parameter values are in the Appendix 5.1.

We quantified the pointwise estimation accuracy and variance of our estimator, as summarized in Table 1. Overall, both methods recover the fixed effects $\log(\vartheta_1)$ and $\log(\vartheta_2)$ well, as indicated by small relative biases and low RRMSE values. In contrast, the inter-individual variability parameter ω_{ϑ_1} , exhibits larger RRMSEs and relative biases than the fixed-effect parameters, reflecting the greater difficulty of estimating random-effect variance components from sparse per-subject sampling. Finally, the close agreement between empirical and estimated variances and the near-nominal coverage probabilities (≈ 0.95) suggest that the uncertainty quantification provided by both methods is reasonably well calibrated in this setting. Moreover, we verified that our method does not introduce additional practical identifiability issues in Figure 1. This first example is a simple one for which SAEM based approach is known to succeed. It illustrates our method's ability to retrieve the same accuracy level as classic methods for problem of reasonable complexity.

3.2 Antibody kinetics

3.2.1 Simulation setting

We designed a second simulation study to assess the performance of our VAE-based inference framework: a partially observed NLME-ODEs describing antibody kinetics following multiple vaccine injections developed in [Clairon et al. \(2023\)](#). The mechanistic model for the given

Parameter	Method	Rel. Bias (%)	RRMSE (%)	Emp. Var. (10^{-2})	Est. Var. (10^{-2})	Emp. Cov.	Est. Cov.
$\log(\vartheta_1)$	VAE	1.04	6.58	0.20	0.25	0.95	0.96
	SAEM	-0.50	7.24	0.25	0.25	0.94	0.94
$\log(\vartheta_2)$	VAE	-0.10	2.63	0.03	0.04	0.94	0.95
	SAEM	0.04	2.64	0.03	0.03	0.95	0.95
ω_{ϑ_1}	VAE	2.56	10.42	0.49	0.56	0.94	0.97
	SAEM	2.39	10.35	0.49	0.50	0.94	0.95
σ_ϵ	VAE	-0.31	1.42	0.21	0.27	0.94	0.95
	SAEM	-0.07	1.97	0.40	0.41	0.94	0.94

Table 1: Comparison of parameter estimates for the pharmacokinetic model in 3.1 obtained with the VAE and SAEM methods.

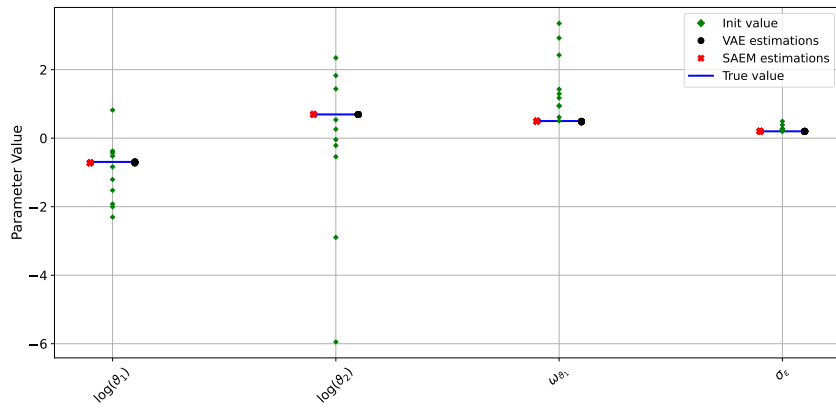


Figure 1: Convergence assessment of SAEM and VAE in pharmacokinetic model. For each parameter, we show the scatter of estimates over random initializations. A single tight cluster around the true value indicates identifiability, whereas multiple separated clusters reveal competing local optima and lack of robustness.

i -th subject is defined as:

$$\begin{cases} \dot{S}_i(t) = \bar{f}_{M_{k,i}} e^{-\delta_V(t-t_k)} - \delta_S S_i(t), \\ \dot{A}b_i(t) = \vartheta_i S_i(t) - \delta_{Ab} A b_i(t), \\ (S_i(0), A b_i(0)) = (0.01, 0.1) \end{cases} \quad (12)$$

with three injection times $t_{k=1,2,3}$. The above system represents a two-compartment mechanistic model capturing the post-vaccination antibody response dynamics. The state variable

S_i denotes the secreting cells population responsible for antibody production, while Ab_i denotes blood circulating antibody concentration. The parameters \bar{f}_{M_k} represents the fold-change of B-cells population magnitude able to differentiate into secreting cells after k -th injection compared to the first one (by definition $\bar{f}_{M_{1,i}} = 1$). The decay rate δ_S controls the lifespan of the secreting cell population, and δ_{Ab} governs the antibody degradation rate. In this ODEs, δ_V is the degradation rate of the vaccine induced antigen. The parameter ϑ_i represents the subject-specific antibody production rate per secreting cells, capturing inter-individual variability in immune response intensity. The pair (δ_S, δ_{Ab}) is not structurally identifiable when relying solely on Ab_i observations. To break the symmetry that causes structural non-identifiability, we impose the constraint: $\log(\delta_{Ab}) = \log(\delta_S + \exp(\lambda))$, where $\lambda \in \mathbb{R}$ is a log-gap parameter controlling the difference between the two decay rates and enforcing $\delta_{Ab} > \delta_S$ in the ODEs Eq. 12 (more details in Appendix Section 3).

Inter-individual variability is introduced in the parameters ϑ_i and $\bar{f}_{M_{2,i}}$ according to

$$\log(\vartheta_i) = \log(\vartheta) + b_{\vartheta,i}, \quad b_{\vartheta,i} \sim \mathcal{N}(0, \omega_{\vartheta}^2),$$

$$\log(\bar{f}_{M_{2,i}}) = \log(\bar{f}_{M_2}) + b_{\bar{f}_{M_2,i}}, \quad b_{\bar{f}_{M_2,i}} \sim \mathcal{N}(0, \omega_{\bar{f}_{M_2,i}}^2),$$

where ϑ and \bar{f}_{M_2} are shared across the population. In this system, only the antibody compartment is observed, whereas the upstream driver of the dynamics remains unmeasured. The observed antibody concentration is related to the latent state through a log-transformed observation model with σ_{Ab} :

$$Y_{Ab,ij} = \log_{10} Ab_{ij}(t_{ij}) + \epsilon_{Ab,ij}, \quad \epsilon_{Ab,ij} \sim \mathcal{N}(0, \sigma_{Ab}^2).$$

We generated two sets of datasets: 100 datasets with 15 measurements per subject collected at equally spaced time points, and 100 datasets with 10 measurements per subject collected at irregular time points over the 400-day follow-up as illustrated in Figure 2(b) and (c). Each dataset consists of 50 subjects. The true parameter values are in the Appendix 5.2.

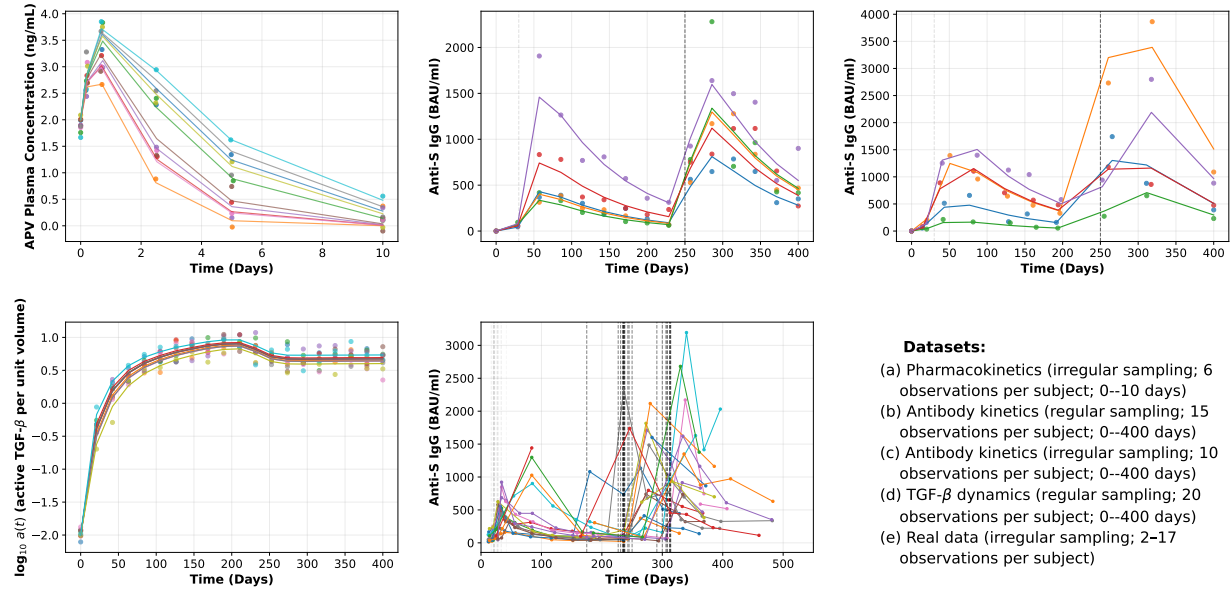


Figure 2: Randomly selected subject trajectories from the simulated datasets and the real dataset. Points are noisy observations; solid curves show the corresponding noise-free underlying dynamics. Vertical light-grey and black dashed lines mark the second and third vaccine injections (the first occurs at $t=0$).

3.2.2 Estimation scenario

The parameters such as δ_S and \bar{f}_{M_k} affect the observations only indirectly. Moreover, compensatory effects between δ_{Ab} and δ_S can induce strong correlations in their estimates, further impairing identifiability. We therefore consider three inference scenarios of increasing dimensionality, reflecting progressively more complex settings: (S1) baseline scenario in which we estimate the population parameter: $\phi = (\log(\vartheta), \log(\bar{f}_{M_2}), \log(\bar{f}_{M_3}), \omega_\vartheta, \omega_{\bar{f}_{M_2}}, \sigma_{Ab})$ (S2) scenario S1 augmented with the estimation of the degradation rate of Secreting cells $\log(\delta_S)$ (S3) Scenario S2 is further extended with the antibody decay estimation, $\log(\delta_{Ab})$.

3.2.3 Results and identifiability analysis.

In the sparse regular sampling setting, the VAE approach yields lower or comparable relative bias, RRMSE and variance of the estimations for the population parameters compared to

SAEM, confirming its accuracy in recovering fixed effects in the scenario 1. However, it performs slightly worse for the random-effect variances, where a modest underestimation is observed. This behavior is expected, as variational inference typically produces a tighter posterior approximation that tends to underestimate uncertainty components (Blei et al. 2017). In Scenario 2, SAEM exhibits a clear inconsistency between its estimated variances and the empirical variances computed across the $N_{MC} = 100$ simulated datasets for the mean population parameter $\log(\vartheta)$, $\log(\bar{f}_{M_2})$ and $\log(\bar{f}_{M_3})$. The disagreement can be attributed to the FIM computation in SAEM, which relies on local curvature at the converged point. In this nonlinear setting with correlated parameters, the MCMC-based E-step may mix slowly and drive SAEM toward a suboptimal local basin, where the likelihood appears spuriously sharp in certain directions, resulting in variance underestimation. In the more complex scenario 3, SAEM frequently converges to local minima and fails to recover several parameters as shown in Figure 3(A), preventing replication over $N_{MC} = 100$ datasets. The VAE method, by contrast, remains numerically stable and produces coherent parameter estimates, demonstrating its robustness in moderately ill-conditioned inference regimes.

In the sparse irregular sampling setting, the SAEM algorithm exhibits a loss of practical identifiability across all three scenarios. This behavior becomes more pronounced as the scenarios become more challenging, and is particularly visible for parameters governing the decay dynamics (e.g. δ_S , δ_{Ab}), for which SAEM frequently converges away from the true value. By contrast, the VAE-based method remains stable under the same sparse irregular design. We report only the results for Scenario 3 obtained with the VAE in the Table 3. For SAEM, a non-negligible fraction of simulation runs did not yield reliable standard error estimates because the observed Hessian was singular for key parameters. In particular, in Scenario 2 and Scenario 3, the Hessian blocks associated with δ_S and δ_{Ab} were not invertible for approximately 15% and 20% of the datasets respectively, preventing computation of the

estimated covariance matrix and downstream uncertainty summaries.

Overall, these results confirm that partial observation combined with sparse sampling amplifies the practical identifiability challenges of NLME-ODEs. In such settings, SAEM's reliance on finite-sample MCMC approximations in complex posterior spaces can lead to unstable or biased estimation. The VAE approach, by directly optimising a smoother ELBO, avoids the sampling bottleneck and better preserves identifiability as the parameter space grows.

3.3 Dynamics of TGF Activation in Asthmatic Airways

To further challenge the proposed inference methods, we next consider a more complex ODE system with richer nonlinear interactions. To reproduce the dynamics of airway remodeling, we adopt the reduced system proposed by [Pybus et al. \(2023\)](#), which captures the fast biochemical activation of transforming growth factor β (TGF- β) mediated by airway smooth muscle (ASM) and extracellular matrix (ECM) interactions. The model describes the temporal evolution of the densities of proliferating ASM cells $p(t)$, contractile ASM cells $c(t)$, active TGF- β concentration $a(t)$, and ECM $m(t)$ as follows:

$$\begin{cases} \frac{dp_i}{dt} = \kappa_{pi} p_i \left(1 - \frac{p_i}{p_{\max}}\right) \left(1 + \frac{\kappa_{ap} a_i p_i}{\tilde{\eta}_{ap} + a_i p_i}\right) + \kappa_{cp} \frac{\gamma_c}{\gamma_p} c_i - \kappa_{pc} p_i, \\ \frac{dc_i}{dt} = \kappa_{pc} \frac{\gamma_p}{\gamma_c} p_i - (\kappa_{cp} + \phi_c) c_i, \\ \frac{da_i}{dt} = \left(\frac{\kappa_s}{\nu} e^{-\frac{(t-\tau_i)^2}{\nu^2}} + \frac{\kappa_{ac} a_i c_i}{\tilde{\eta}_{ac} + a_i c_i}\right) \frac{c_i}{m_i} \gamma_a - \kappa_b \left(\frac{\gamma_p}{\gamma_c} p_i + c_i\right) a_i - a_i, \\ \frac{dm_i}{dt} = \left(\kappa_{pm} + \frac{\kappa_{apm} a_i p_i}{\tilde{\eta}_{apm} + a_i p_i}\right) \gamma_p p_i - \phi_m m_i \end{cases} \quad (13)$$

$$(p_i(0), c_i(0), a_i(0), m_i(0)) = (0.1, 0.8, 0.01, 0.9).$$

The design was implemented with one random effect on the kinetic parameter k_p as:

$$\log(k_{p_i}) = \log(k_p) + b_i \quad \text{and} \quad b_i \sim \mathcal{N}(0, \omega_{k_p}^2),$$

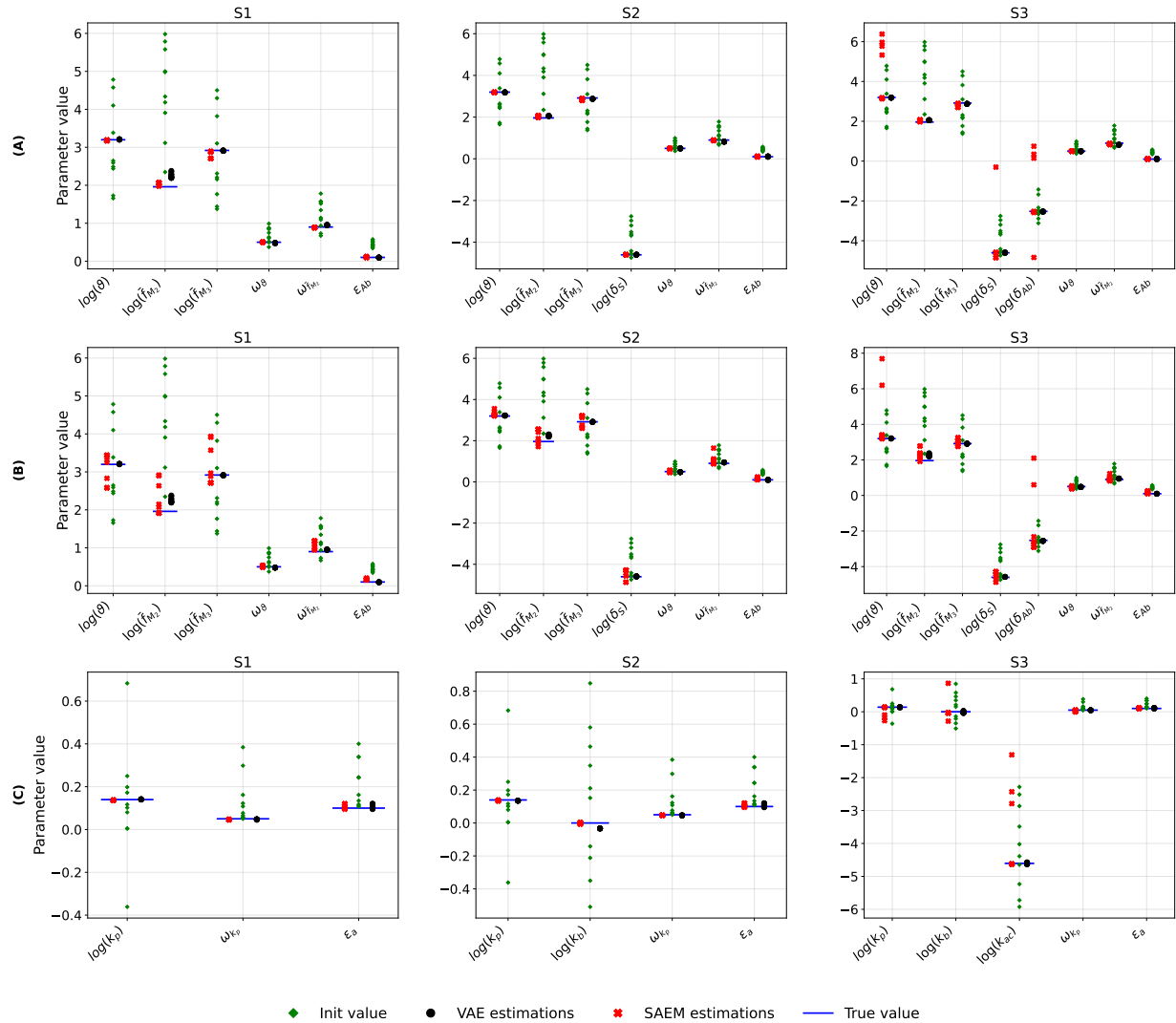


Figure 3: Convergence assessment of SAEM and VAE across three simulation scenarios (S1–S3) for the antibody kinetics and TGF- β dynamics. Columns correspond to scenarios (S1, S2, S3). Rows correspond to the simulation case: (A) antibody kinetics with regular sampling, (B) antibody kinetics with irregular sampling, and (C) TGF- β dynamics. For each parameter, points show estimates obtained from multiple random initializations. A tight cluster around the true value suggests robust convergence, whereas multiple separated clusters indicate competing local optima and sensitivity to initialization.

Table 2: Comparison of parameter estimates on the simulation datasets from the antibody kinetic model in regular sampling design (15 measurements per-subject over 400 days) in the section 3.2 obtained with the VAE and SAEM methods.

Scenario	Parameter	Method	Rel. Bias (%)	RRMSE (%)	Emp. Var. (10^{-2})	Est. Var. (10^{-2})	Emp. Cov.	Est. Cov.
S1	$\log(\vartheta)$	VAE	-0.49	2.46	0.59	0.48	0.96	0.91
		SAEM	-1.08	2.67	0.61	0.61	0.98	0.90
	$\log(\bar{f}_{M_2})$	VAE	1.38	7.12	1.87	1.29	0.94	0.90
		SAEM	1.65	7.22	1.90	1.81	0.95	0.93
	$\log(\bar{f}_{M_3})$	VAE	0.34	1.33	0.14	0.14	0.94	0.94
		SAEM	1.02	1.70	0.16	0.17	0.92	0.77
	ω_ϑ	VAE	-3.67	11.72	0.31	0.21	0.94	0.82
		SAEM	1.36	11.28	0.31	0.26	0.97	0.93
	$\omega_{\bar{f}_{M_2}}$	VAE	-2.41	10.58	0.86	0.68	0.94	0.86
		SAEM	0.11	11.23	1.02	0.88	0.94	0.88
S2	σ_{Ab}	VAE	1.56	2.90	0.06	0.06	0.94	0.94
		SAEM	1.52	3.05	0.07	0.07	0.95	0.94
	$\log(\vartheta)$	VAE	-0.96	2.25	0.42	0.45	0.90	0.90
		SAEM	-0.91	2.55	0.58	1.09	0.98	0.94
	$\log(\bar{f}_{M_2})$	VAE	1.55	6.35	1.46	1.46	0.94	0.90
		SAEM	1.07	7.08	1.90	2.83	0.95	0.95
	$\log(\bar{f}_{M_3})$	VAE	0.60	1.39	0.13	0.14	0.95	0.92
		SAEM	0.78	1.59	0.16	1.15	0.90	0.83
	$\log(\delta_s)$	VAE	0.12	0.39	0.03	0.03	0.95	0.94
		SAEM	0.04	0.44	0.04	0.06	0.94	0.96
S3	ω_ϑ	VAE	-3.01	11.54	0.31	0.20	0.94	0.85
		SAEM	-1.51	10.38	0.26	0.26	0.95	0.95
	$\omega_{\bar{f}_{M_2}}$	VAE	-3.19	10.98	0.89	0.85	0.92	0.88
		SAEM	~0.0	11.32	0.94	0.94	0.94	0.89
	σ_{Ab}	VAE	1.65	3.12	0.07	0.07	0.94	0.94
		SAEM	1.75	3.33	0.08	0.08	0.95	0.94
	$\log(\vartheta)$	VAE	-0.70	2.42	0.55	0.73	0.93	0.93
	$\log(\bar{f}_{M_2})$	VAE	0.62	6.86	1.79	1.46	0.94	0.90
	$\log(\bar{f}_{M_3})$	VAE	0.59	1.38	0.13	0.17	0.95	0.95
	$\log(\delta_s)$	VAE	0.14	0.52	0.05	0.06	0.93	0.95

Scenario	Parameter	Method	Rel. Bias (%)	RRMSE (%)	Emp. Var. (10^{-2})	Est. Var. (10^{-2})	Emp. Cov.	Est. Cov.
S3	$\log(\vartheta)$	VAE	-0.58	3.02	0.89	0.86	0.96	0.95
	$\log(\bar{f}_{M_2})$	VAE	-0.2	6.95	1.85	1.92	0.96	0.97
	$\log(\bar{f}_{M_3})$	VAE	0.14	1.63	0.22	0.29	0.95	0.96
	$\log(\delta_s)$	VAE	0.34	0.52	0.20	0.19	0.98	0.97
	$\log(\delta_{Ab})$	VAE	-1.01	3.82	0.95	0.97	0.98	0.97
	ω_ϑ	VAE	-3.65	12.97	0.39	0.34	0.90	0.87
	$\omega_{\bar{f}_{M_2}}$	VAE	-4.75	14.28	1.46	1.04	0.98	0.88
	σ_{Ab}	VAE	1.68	3.92	2.65	0.69	0.96	0.90

Table 3: Parameter estimates in scenario 3 on 100 irregular sampling simulation datasets (10 measurements per-subject over 400 days) from the antibody kinetic model in the section 3.2 obtained with the VAE.

representing the individual rate of ASM proliferation. Only TGF-beta is observed according to the observation model:

$$Y_{ij} = \log_{10}(a(t_{ij})) + \epsilon_{a,ij}$$

where $\epsilon_{a,ij} \sim \mathcal{N}(0, \sigma_a^2)$ with 20 longitudinal measurements uniformly distributed over 400 days, example of randomly drawn data are represented in Figure 2. Each dataset consists of 50 subjects. The true parameters are in the Appendix Table 2.

3.3.1 Estimation scenarios

The inference task is made difficult by the strongly coupled, feedback-rich ODE structure (logistic proliferation, phenotype switching, Hill-type saturations, and multiplicative terms such as $a_i c_i$), which induces nonconvex likelihoods, strong parameter interactions, and practical near-nonidentifiabilities. We consider three inference scenarios of increasing dimensionality: (S1) a baseline setting estimating $\phi = \{\log(k_p), \omega_{k_p}, \sigma_a\}$; (S2) S1 augmented by estimating $\log(k_b)$; and (S3) S2 further extended by estimating $\log(k_{ac})$.

3.3.2 Results

As shown in Table 4, the VAE approach consistently outperforms SAEM, with smaller relative bias and lower RRMSE across all parameters. Regarding practical identifiability (Figure 3C), parameters appear identifiable in Scenarios 1–2, but SAEM becomes unstable in Scenario 2: FIM-based coverage for k_b drops to 2% due to severe variance underestimation. This likely reflects a challenging nonconvex likelihood, causing SAEM to converge to suboptimal regions with spuriously high curvature in the k_b direction. As a result, empirical variance is much larger (empirical coverage 86%), while VAE provides more stable estimates and uncertainty, especially for k_b .

The scenario 3 lead to more complex setting: adding k_{ac} strengthens the positive feedback $a \uparrow \Rightarrow c \uparrow, m \uparrow \Rightarrow a \uparrow$, increasing effective stiffness and deepening nonconvexity. VAE remains stable with acceptable bias and coverage, whereas SAEM loses practical identifiability, consistent with well-known challenges of SAEM on stiff, highly nonlinear NLME-ODEs when curvature is poorly conditioned. We do not execute SAEM over the 100 simulated datasets in this scenario.

Overall, these experiments confirm that the proposed VAE approach can handle the nonlinear, partially stiff dynamics of the TGF- β activation with reasonable accuracy and calibrated uncertainty, even when SAEM becomes numerically unstable.

4 Application on real data

In the real data case, we relied on data from a cohort of Bnt162b2 vaccine recipients, in which both antibody kinetics and neutralizing activity were measured longitudinally against SARS-CoV-2. In brief, SARS-CoV-2 naive patients were recruited in Orléans, France between August 27, 2020 and May 24, 2022. Individuals were followed for up to 483 days

Scenario	Parameter	Method	Rel. Bias (1%)	RRMSE (1%)	Emp. Var. (1%)	Est. Var. (1%)	Emp. Cov.	Est. Cov.
S1	$\log(k_p)$	VAE	-0.27	4.89	0.0047	0.0061	0.95	0.97
		SAEM	-2.61	5.47	0.0045	0.0052	0.90	0.92
	ω_{k_p}	VAE	~ 0.0	7.68	0.0015	0.0040	0.95	0.97
		SAEM	-4.45	10.60	0.0023	0.0030	0.94	0.96
	σ_a	VAE	1.65	3.12	0.07	0.07	0.94	0.94
		SAEM	1.75	3.33	0.08	0.08	0.95	0.94
S2	$\log(k_p)$	VAE	0.37	6.21	0.010	0.009	0.96	0.95
		SAEM	0.97	6.40	0.008	0.006	0.90	0.90
	k_b	VAE	0.03	1.29	0.010	0.019	0.94	0.96
		SAEM	1.40	1.90	0.020	0.0002	0.90	0.02
	ω_{k_p}	VAE	-0.07	9.44	0.002	0.004	0.94	0.97
		SAEM	-1.75	9.99	0.002	0.003	0.93	0.98
	σ_a	VAE	1.55	3.07	0.07	0.07	0.94	0.94
		SAEM	1.45	3.18	0.08	0.08	0.95	0.94
S3	$\log(k_p)$	VAE	1.12	6.48	0.01	0.009	0.94	0.93
	k_b	VAE	1.45	2.56	0.07	0.1	0.94	0.96
	$\log(k_{ac})$	VAE	0.29	0.50	0.04	0.09	0.89	0.97
	ω_{k_p}	VAE	-1.85	9.20	0.002	0.005	0.94	0.95
	σ_a	VAE	1.55	3.07	0.07	0.07	0.94	0.94

Table 4: Comparison of parameter estimates on the simulation datasets from dynamics of TGF- β activation in section 3.3 obtained with the VAE and SAEM methods.

after their first vaccine injections (see more details on the data in (Planas et al. 2021)). The data pre-treatment and selection process is exactly the same as in Clairon et al. (2023). We used only the antibody kinetics data in the original dataset and analysed $N = 25$ subjects who received three injections. The evolution of antibody titers (BAU/ml) is shown in Figure 2 over a 500-day period. For the analysis of this dataset, we employed exactly the same model design as the simulation study in the section 3.2. We estimate the following parameter set: $\phi = \{\log(\vartheta), \log(\bar{f}_{M_2}), \log(\bar{f}_{M_3}), \log(\delta_S), \log(\delta_{Ab}), \omega_\vartheta, \omega_{\bar{f}_{M_2}}, \sigma_\epsilon\}$,

Parameter	VAE			SAEM		
	Est.	95% CI Lower	95% CI Upper	Est.	95% CI Lower	95% CI Upper
$\log(\vartheta)$	3.68	3.56	3.81	3.62	3.05	4.19
$\log(\bar{f}_{M_2})$	1.36	1.32	1.40	1.35	1.01	1.69
$\log(\bar{f}_{M_3})$	2.51	2.48	2.54	2.62	2.31	2.93
$\log(\delta_S)$	-4.72	-4.74	-4.70	-4.72	-4.92	-4.51
$\log(\delta_{Ab})$	-1.89	-2.09	-1.69	-1.91	-2.61	-1.21
ω_ϑ	0.47	0.32	0.61	0.46	0.34	0.58
$\omega_{\bar{f}_{M_2}}$	0.07	0.05	0.08	0.17	0.04	0.31
σ_ϵ	0.22	0.21	0.23	0.21	0.19	0.23

Table 5: VAE and SAEM parameter estimates and 95% CIs on real dataset

4.1 Results

Table 5 reports the estimates on the real dataset obtained with both methods. Overall, the two methods provide consistent estimates for the population parameters and observation noise, with all corresponding 95% confidence intervals overlapping. The main difference appears in the random-effect variance associated with \bar{f}_{M_2} , where the VAE estimate is smaller than that obtained by SAEM. Nevertheless, the confidence intervals still overlap, indicating no statistically significant discrepancy. A plausible explanation is limited identifiability of the random-effect variance for \bar{f}_{M_2} in the real dataset. In such settings, different inference schemes may yield similar population means while producing more variable estimates of variance components. The smaller VAE estimate is consistent with the well-known tendency of variational inference to underestimate posterior uncertainty, but the overlapping confidence intervals suggest that the data do not strongly distinguish between the two estimates. As shown in Figure 5, the VAE and SAEM yielded consistent parameter estimates regardless of starting points.

At the population level without accounting for interindividual random effects, Figure 4 compares the estimated population mean trajectories obtained by the VAE and SAEM

approaches. For the antibody kinetic, the VAE-based trajectory provides a more accurate reconstruction: the SAEM trajectory consistently falls within the 95% prediction interval of the VAE approach. This indicates that the variational approach captures the underlying uncertainty more faithfully, while SAEM remains well-aligned but more dispersed. For the secreting cells, however, a small discrepancy appears in the peak region after 3rd injection, where SAEM deviates outside the VAE related confidence interval. Figure 5 illustrates individual predictive trajectories under the VAE-based NLME–ODEs, generated using the mode of the variational posterior for the subject-specific random effects b_i . The predicted means match the observed data, and the 95% prediction intervals show good overall coverage, confirming that the variational posterior captures the main sources of individual uncertainty.

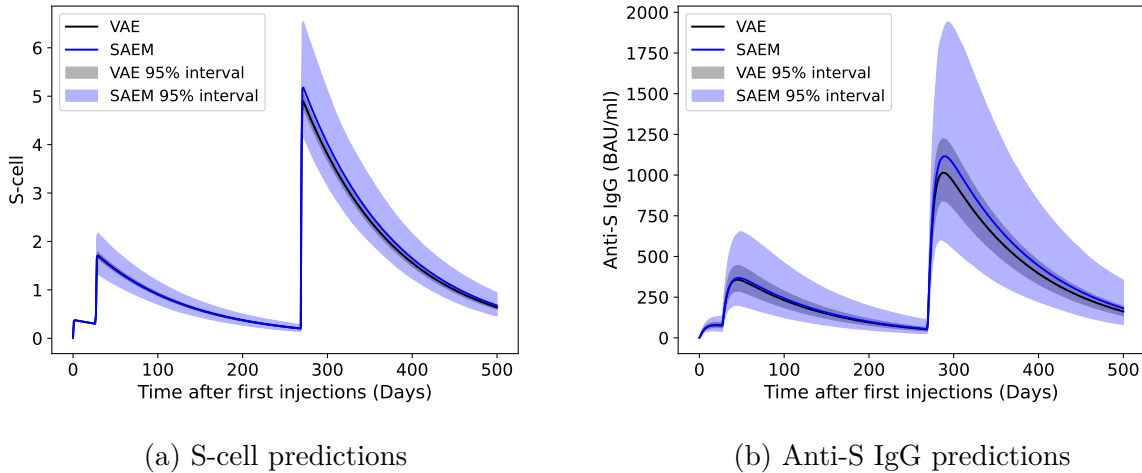


Figure 4: Real-world dataset: population mean predictions (CI band 95%)

5 Discussion

In this work, we use a variational autoencoder for parameter inference in NLME–ODE models, replacing the sampling step in classical methods such as SAEM. The random-

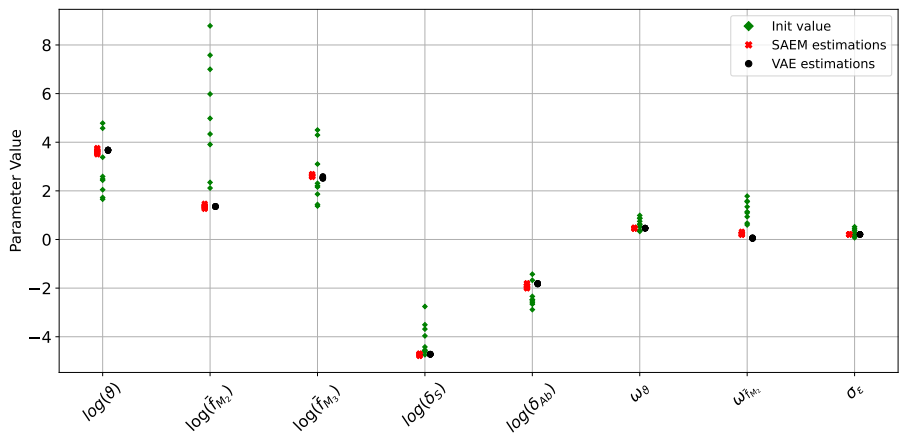
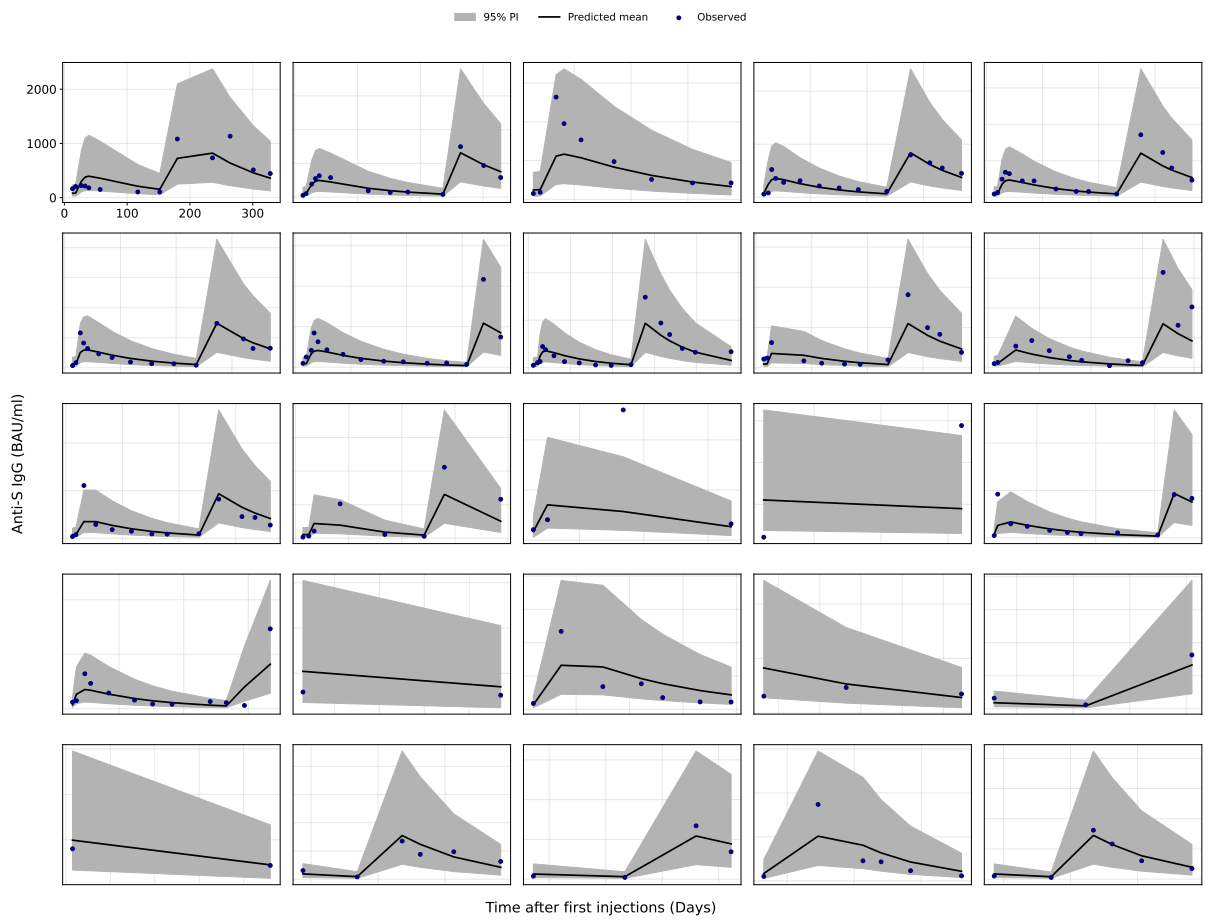


Figure 5: Real-world dataset: individual VAE predictions (top) and parameter identifiability (bottom).

effects posterior is approximated by a Gaussian variational distribution parameterized by a lightweight amortized encoder, designed for sparse biological and clinical datasets. Throughout the design, particular attention was devoted to practical identifiability to ensure that the introduction of variational parameters does not compromise the interpretability of the model. For uncertainty quantification, we evaluate the observed FIM via direct hessian of Monte Carlo approximated marginal likelihood using prior-based reparametrization and automatic differentiation. In terms of estimation accuracy, for fixed-effect parameters, our variational method achieved performance comparable to SAEM on real data and outperformed it in more challenging simulated scenarios involving stronger nonlinearities, partial observation. As the number of population parameters increases, the performance gap widened in favor of the variational approach, illustrating its robustness to the increased curvature and multimodality of the likelihood surface—conditions under which SAEM often suffers from slow convergence or attraction to suboptimal local maxima. Both the empirical coverage and the coverage predicted from the estimated variances remained generally close to the nominal 95% level, especially for the fixed effect parameters.

Future extensions could focus on increasing the flexibility and robustness of the variational approximation. One direction is to enrich the variational posterior, either through more expressive encoder architectures or structured variational families such as normalizing flows, to alleviate underestimation of random-effect variances and better capture posterior correlations. Another avenue is to move toward a fully variational Bayes formulation by placing priors on the population-level parameters, thereby propagating uncertainty across both fixed and random effects and enabling a more coherent Bayesian interpretation. These extensions are also expected to mitigate the over-confidence of standard variational inference by allowing a better match to the true posterior. Beyond this, applying the framework to higher-dimensional mechanistic models with covariates or censored data, including systems

with more ODE states or large sets of random effects, would further assess its scalability and amortization efficiency. Extending the methodology to semi-parametric or partially nonparametric formulations, for instance via neural augmentations of ODE components, also raises new identifiability challenges whose interaction with variational regularization deserves careful study. Finally, a theoretical analysis of the estimator, encompassing conditions for consistency and asymptotic normality of the ELBO maximizer, stability of the amortized inference map would strengthen the statistical foundations of the proposed approach.

Acknowledgments

This work receives financial support from Inserm to the booster program Exposome, also has been supported by SOLVE, funded by the European Union’s Horizon Europe Research and Innovation programme under grant n°101137185. We are deeply thankful to Delphine Planas, Timothée Bruel, Laurent Hocqueloux, Thierry Prazuck and Olivier Schwartz for the production and the public availability of the data used in section 4. The experiments presented in this paper were carried out using the PlaFRIM experimental testbed, supported by Inria, CNRS (LABRI and IMB), Université de Bordeaux, Bordeaux INP and Conseil Régional d’Aquitaine (see <https://www.plafrim.fr>). We thank Simulations Plus, Lixoft division for the free academic use of the MonolixSuite.

SUPPLEMENTARY MATERIAL

Supplementary text: Supplementary material is provided as a separate pdf document.

Code and data: Code and data are available at https://github.com/AuroraFr/NN_NLME/tree/paper

6 Disclosure statement

The authors declare no conflicts of interest.

References

Arruda, G. F., Dondelinger, F. & Hasenclever, L. (2024), An amortized approach to nonlinear mixed-effects modeling based on neural posterior estimation, *in* ‘Proceedings of the 41st International Conference on Machine Learning (ICML)’, Vol. 235 of *Proceedings of Machine Learning Research*, PMLR, pp. 10703–10723.

Audoly, S., Bellu, G., D’Angio, L., Saccomani, M. P. & Cobelli, C. (2001), ‘Global identifiability of nonlinear models of biological systems’, *IEEE Transactions on Biomedical Engineering* **48**(1), 55–65.

Bellman, R. & Åström, K. J. (1970), ‘On structural identifiability’, *Mathematical Biosciences* **7**, 329–339.

Blei, D. M., Kucukelbir, A. & McAuliffe, J. D. (2017), ‘Variational inference: A review for statisticians’, *Journal of the American Statistical Association* **112**(518), 859–877.

Bräm, D. S., Steiert, B., Pfister, M., Steffens, B. & Koch, G. (2025), ‘Low-dimensional neural ordinary differential equations accounting for inter-individual variability implemented in monolix and nonmem’, *CPT: Pharmacometrics & Systems Pharmacology* **14**, 5–16.

Carpenter, B., Gelman, A., Hoffman, M. D., Lee, D., Goodrich, B., Betancourt, M., Brubaker, M., Guo, J., Li, P. & Riddell, A. (2017), ‘Stan: A probabilistic programming language’, *Journal of Statistical Software* **76**(1), 1–32.

Clairon, Q., Prague, M., Planas, D., Bruel, T., Hocqueloux, L., Prazuck, T., Schwartz, O., Thiébaut, R. & Guedj, J. (2023), ‘Modeling the kinetics of the neutralizing antibody

response against sars-cov-2 variants after several administrations of bnt162b2’, *PLoS Computational Biology* **19**(8), e1011282.

Dai, B., Wang, Z. & Wipf, D. (2020), The usual suspects? reassessing blame for VAE posterior collapse, *in* ‘Proceedings of the 37th International Conference on Machine Learning’, Vol. 119, pp. 2313–2322.

Delyon, B., Lavielle, M. & Moulines, E. (1999), ‘Convergence of a stochastic approximation version of the em algorithm’, *Annals of Statistics* **27**(1), 94–128.

Google DeepMind (2020), ‘Optax: A gradient processing and optimization library for jax’, <https://github.com/google-deepmind/optax>.

Janssen, A., Bennis, F. C., Cnossen, M. H. & Mathôt, R. A. A. (2024), ‘Mixed effect estimation in deep compartment models: Variational methods outperform first-order approximations’, *Journal of Pharmacokinetics and Pharmacodynamics* **51**, 797–808.

Kidger, P. (2022), ‘Diffrax: Neural differential equations on jax’, <https://docs.kidger.site/diffrax/>.

Kingma, D. P. & Ba, J. (2015), Adam: A method for stochastic optimization, *in* ‘International Conference on Learning Representations (ICLR)’.

Kingma, D. P. & Welling, M. (2014), Auto-encoding variational bayes, *in* ‘International Conference on Learning Representations (ICLR)’.

Lavielle (2014), *Mixed Effects Models for the Population Approach: Models, Tasks, Methods and Tools*, Chapman & Hall/CRC Biostatistics Series, Chapman and Hall/CRC.

Lavielle, M. & Aarons, L. (2016), ‘What do we mean by identifiability in mixed effects models?’, *Journal of Pharmacokinetics and Pharmacodynamics* **43**(1), 111–122.

Lavielle, M. & Mentré, F. (2007), ‘Estimation of population pharmacokinetic parameters of

saquinavir in hiv patients with the monolix software', *Journal of Pharmacokinetics and Pharmacodynamics* **34**(2), 229–249.

Lixoft-SAS (2025), 'Monolix suite 2025', <https://lixoft.com>. Software, version 2025R1.

Lunn, D. J., Thomas, A., Best, N. & Spiegelhalter, D. (2000), 'Winbugs—a bayesian modelling framework: concepts, structure, and extensibility', *Statistics and Computing* **10**(4), 325–337.

Margossian, C. C. & Blei, D. M. (2024), 'Amortized variational inference: When and why?', *Proceedings of the Fortieth Conference on Uncertainty in Artificial Intelligence* **244**, 2434–2449.

Martensen, C. J., Korsbo, N., Ivaturi, V. & Sager, S. (2024), 'Data-driven discovery of feedback mechanisms in acute myeloid leukaemia: Alternatives to classical models using deep nonlinear mixed effect modeling and symbolic regression', *bioRxiv* . Preprint, CC-BY-ND 4.0 license.

Pinheiro, J. C. & Bates, D. M. (1994), 'Approximations to the log-likelihood function in the nonlinear mixed-effects model', *Journal of Computational and Graphical Statistics* **3**(4), 749–762.

Pinheiro, J. C. & Bates, D. M. (2000), *Mixed-Effects Models in S and S-PLUS*, Statistics and Computing, Springer-Verlag, New York.

Planas, D., Veyer, D., Baidaliuk, A., Staropoli, I., Guivel-Benhassine, F., Rajah, M. M. & et al. (2021), 'Reduced sensitivity of sars-cov-2 variant delta to antibody neutralization', *Nature* **596**(7871), 276–280.

Prague, M., Commenges, D., Drylewicz, J. & Thiébaut, R. (2013), 'Assessment of dynamical model for hiv dynamics using a posteriori estimates of the parameters', *Statistics in Medicine* **32**(23), 3899–3910.

Pumas-AI (2025), ‘Pumas® 2.3’, <https://pumas.ai>. Software.

PumasAI (2025), ‘Deeppumas’, <https://deeppumas-docs.pumas.ai/>. Software.

Pybus, H. J. et al. (2023), ‘A dynamical model of tgf- β activation in asthmatic airways’, *IMA Journal of Mathematics Applied in Medicine and Biology* .

Qian, Z., Zame, W. R., Fleuren, L. M., Elbers, P. & van der Schaar, M. (2021), Integrating expert odes into neural odes: Pharmacology and disease progression, in ‘Proceedings of the 35th Conference on Neural Information Processing Systems (NeurIPS)’.

Raue, A., Kreutz, C., Maiwald, T., Bachmann, J., Schilling, M., Klingmüller, U. & Timmer, J. (2009), ‘Structural and practical identifiability analysis of partially observed dynamical models by exploiting the profile likelihood’, *Bioinformatics* **25**(15), 1923–1929.

Roeder, G., Grant, P. K., Phillips, A., Dalchau, N. & Meeds, E. (2019), Efficient amortised bayesian inference for hierarchical and nonlinear dynamical systems, in ‘Proceedings of the 36th International Conference on Machine Learning (ICML)’, Vol. 97 of *Proceedings of Machine Learning Research*, PMLR, Long Beach, California, USA, pp. 4448–4458.

Rohleff, J., Bachmann, F., Nahum, U., Bräm, D., Steffens, B., Pfister, M., Koch, G. & Schropp, J. (2025), ‘Redefining parameter estimation and covariate selection via variational autoencoders: One run is all you need’, *CPT: Pharmacometrics & Systems Pharmacology* **14**(12), 2232–2243.

Vaswani, A., Shazeer, N., Parmar, N., Uszkoreit, J., Jones, L., Gomez, A. N., Kaiser, Ł. & Polosukhin, I. (2017), Attention is all you need, in ‘Advances in Neural Information Processing Systems’, Vol. 30.

Wang, Y., Blei, D. M. & Cunningham, J. P. (2021), Posterior collapse and latent variable non-identifiability, in ‘Advances in Neural Information Processing Systems’.

SUPPLEMENTARY MATERIAL

1 ELBO formulation

$$\mathcal{L}_{\text{elbo}_i}(\phi, \psi; Y_i) = \underbrace{\mathbb{E}_{q_\psi(b_i|Y_i)}[\log p_\phi(Y_i | b_i)]}_{\text{data fidelity}} - \underbrace{\text{KL}(q_\psi(b_i | Y_i) \| p_\phi(b_i))}_{\text{regularization}}. \quad (1)$$

Assuming the independence between the subjects, ELBO objective function is developed as following:

$$\begin{aligned} \ln p_\phi(Y) &= \sum_{i=1}^n \ln \int_{\mathbb{R}^D} p_\phi(Y_i | b_i) \frac{p_\phi(b_i)}{q_\psi(b_i | Y_i)} q_\psi(b_i | Y_i) db_i \\ &= \sum_i \ln \mathbb{E}_{b_i \sim q_\psi(\cdot | Y_i)} \left[p_\phi(Y_i | b_i) \frac{p_\phi(b_i)}{q_\psi(b_i | Y_i)} \right] \\ &\geq \sum_i \mathbb{E}_{b_i \sim q_\psi(\cdot | Y_i)} [\ln p_\phi(Y_i | b_i)] + \mathbb{E}_{b_i \sim q_\psi(\cdot | Y_i)} \left[\ln \frac{p_\phi(b_i)}{q_\psi(b_i | Y_i)} \right] \\ &= \sum_i \mathbb{E}_{b_i \sim q_\psi(\cdot | Y_i)} [\ln p_\phi(Y_i | b_i)] - KL(q_\psi(\cdot | Y_i) || p_\phi(\cdot)) \\ &\approx \sum_i \frac{1}{L} \sum_{l=1}^L \left[\ln p_\phi(Y_i | b_i^{(l)}) \right] - KL(q_\psi(\cdot | Y_i) || p_\phi(\cdot)) \end{aligned}$$

Data fidelity term The first term in the ELBO given in Equation 1 is the expected log-likelihood under the approximate posterior. It is approximated via Monte-Carlo procedure by drawing samples b_i from q_ψ and averaging the results. It can be made differentiable with respect to all its parameters (ϕ and ψ) using techniques like the reparameterization trick:

$$b_i^{(\ell)} = \mu_\psi(Y_i) + \Sigma_\psi(Y_i) \varepsilon^{(\ell)}, \quad p_{\varepsilon^{(\ell)}} \sim \mathcal{N}(0, I_{D_b}). \quad (2)$$

So, each sampled random effect $b_i^{(\ell)}$ induces a realization of the subject-specific parameter through the mapping: $\theta_i^{(\ell)} = g(\theta, b_i^{(\ell)})$. For each Monte-Carlo sample ℓ , the ODEs defining the latent trajectory $X_i^{(\ell)}$ is solved with parameters $\theta_i^{(\ell)}$. Given $X_i^{(\ell)}$, the likelihood of observed data Y_{ij} is

$$Y_{ij} \sim p_\phi(Y_{ij} | b_i^{(\ell)}) = \mathcal{N}\left(Y_{ij} - h_{\theta_i^{(\ell)}}(X_i^{(\ell)}(t_{ij})), \Sigma\right), \quad j = 1, \dots, n_i.$$

Thus, the expected log-likelihood term appearing in the ELBO is approximated by

$$\begin{aligned} \mathbb{E}_{q_\psi(b_i | Y_i)}[\log p_\phi(Y_i | b_i)] &\approx \frac{1}{L} \sum_{\ell=1}^L \sum_{j=1}^{n_i} \log p_\phi(Y_{ij} | h_{\theta_i^{(\ell)}}(X_i^{(\ell)}(t_{ij})), \Sigma) \\ &\propto -\frac{n_i}{2} \sum_r \log \sigma_{\varepsilon,r}^2 - \frac{1}{2L} \sum_{\ell=1}^L \sum_{j=1}^{n_i} (Y_{ij} - h_{\theta_i^{(\ell)}}(X_i^{(\ell)}(t_{ij})))^\top \Sigma^{-1} (Y_{ij} - h_{\theta_i^{(\ell)}}(X_i^{(\ell)}(t_{ij}))). \end{aligned} \quad (3)$$

Here, L denotes the number of samples drawn from the standard gaussian distribution. A larger L generally improves the accuracy of the ELBO estimation and reduces the variance of the stochastic gradient, but it also increases the computational cost per iteration proportionally because $X_i^{(l)}(t)$ depends on $b_i^{(l)}$ through the ODEs, this expectation requires solving the ODEs for each sample $b_i^{(l)}$. In practice, moderate values of L (e.g., 10–50) often provide a good trade-off between estimation precision and runtime efficiency.

KL divergence term The second term is the Kullback–Leibler divergence between the variational distribution q_ψ and the prior distribution of the random effects p_ϕ , which penalizes deviations from the population-level distribution and thus controls the complexity of the learned individual posteriors. This term has an analytical expression in our case. Let $\sigma_{\psi,d}(Y_i)$ denote the d -th diagonal entry of $\Sigma_\psi(Y_i)$,

$$\text{KL}(q_\psi(b_i | Y_i) \| p_\phi(b_i)) = \int q_\psi(b_i | Y_i) (\log q_\psi(b_i | Y_i) - \log p_\phi(b_i)) db_i \quad (4)$$

$$= \frac{1}{2} \sum_{d=1}^{D_b} \left[\frac{\sigma_{\psi,d}^2(Y_i)}{\omega_d^2} + \frac{\mu_{\psi,d}^2(Y_i)}{\omega_d^2} - 1 + \log(\omega_d^2) - \log(\sigma_{\psi,d}^2(Y_i)) \right]. \quad (5)$$

Altogether, this variational formulation turns the inference task into a tractable optimization problem over (ϕ, ψ) . In the following section, we detail how the variational distribution $q_\psi(b_i | Y_i)$ is parameterized by a neural encoder and how it interfaces with the ODEs-based decoder within our variational inference framework.

Then, the expected log-prior is:

$$\begin{aligned} \int q_\psi(b | Y_i) \log p_\phi(b) db &= \int \mathcal{N}(\mu_\psi(Y_i), \Sigma_\psi(Y_i) \Sigma_\psi(Y_i)^\top) \log \mathcal{N}(\mathbf{0}, \Omega) db \\ &= -\frac{D_b}{2} \log(2\pi) - \frac{1}{2} \sum_{d=1}^{D_b} \left(\log(\omega_{b,d}^2) + \frac{\mu_{\psi,d}^2(Y_i) + \sigma_{\psi,d}^2(Y_i)}{\omega_{b,d}^2} \right) \end{aligned}$$

The expected log-posterior (negative entropy) is:

$$\begin{aligned} \int q_\psi(b \mid Y_i) \log q_\psi(b \mid Y_i) db &= \int \mathcal{N}(\mu_\psi(Y_i), \Sigma_\psi(Y_i)\Sigma_\psi(Y_i)^\top) \log \mathcal{N}(\mu_\psi(Y_i), \Sigma_\psi(Y_i)\Sigma_\psi(Y_i)^\top) db \\ &= -\frac{D_b}{2} \log(2\pi) - \frac{1}{2} \sum_{d=1}^{D_b} (1 + \log(\sigma_{\psi,d}^2(Y_i))) \end{aligned}$$

Therefore, the KL divergence is:

$$\begin{aligned} KL(q_\psi(b_i \mid Y_i) \| p_\phi(b_i)) &= \int q_\psi(b_i) (\log q_\psi(b_i \mid Y_i) - \log p_\phi(b_i)) db_i \\ &= \frac{1}{2} \sum_{d=1}^{D_b} \left[\frac{\sigma_{\psi,d}^2(Y_i)}{\omega_d^2} + \frac{\mu_{\psi,d}^2(Y_i)}{\omega_d^2} - 1 + \log(\omega_d^2) - \log(\sigma_{\psi,d}^2(Y_i)) \right]. \end{aligned}$$

2 Uncertainty quantification

To evaluate $p_{\hat{\phi}}(Y_i)$ and its derivatives, we apply a Monte Carlo approximation based on the reparameterization trick. We express the random effects b_i as a transformation of a noise variable $p_\epsilon \sim \mathcal{N}(\mathbf{0}, I_{D_b})$ independent of ϕ : $b_i = \mathcal{T}_{\hat{\phi}}(\epsilon) = \hat{\Omega}^{1/2}\epsilon$ where $\hat{\Omega}^{1/2}$ is the estimated standard deviation matrix of the prior distribution $p_{\hat{\phi}}(b_i)$ which is assumed to be a zero-mean Gaussian. So we can approximate the marginal likelihood using monte carlo as:

$$p_{\hat{\phi}}(Y_i) \approx \frac{1}{L} \sum_{\ell=1}^L p_{\hat{\phi}}(Y_i \mid b_i^{(\ell)}) = \frac{1}{L} \sum_{\ell=1}^L p_{\hat{\phi}}(Y_i \mid \mathcal{T}_{\hat{\phi}}(\epsilon^{(\ell)})), \quad p_{\epsilon^{(\ell)}} \sim \mathcal{N}(\mathbf{0}, I_{D_b}). \quad (6)$$

The corresponding gradient and Hessian of the marginal likelihood are:

$$\nabla_\phi p_{\hat{\phi}}(Y_i) = \mathbb{E}_{p(\epsilon)} [\nabla_\phi p_{\hat{\phi}}(Y_i \mid \mathcal{T}_{\hat{\phi}}(\epsilon))] \approx \frac{1}{L} \sum_{\ell=1}^L \nabla_\phi p_{\hat{\phi}}(Y_i \mid \mathcal{T}_{\hat{\phi}}(\epsilon^{(\ell)})),$$

$$\nabla_\phi^2 p_{\hat{\phi}}(Y_i) = \mathbb{E}_{p(\epsilon)} [\nabla_\phi^2 p_{\hat{\phi}}(Y_i \mid \mathcal{T}_{\hat{\phi}}(\epsilon))] \approx \frac{1}{L} \sum_{\ell=1}^L \nabla_\phi^2 p_{\hat{\phi}}(Y_i \mid \mathcal{T}_{\hat{\phi}}(\epsilon^{(\ell)})).$$

Now, we can rely on previously used gradient backpropagation techniques to efficiently appproximates $\nabla_\phi p_{\hat{\phi}}(Y_i)$ and $\nabla_\phi^2 p_{\hat{\phi}}(Y_i)$ thanks to the identities:

$$p_{\hat{\phi}}(Y_i \mid \mathcal{T}_{\hat{\phi}}(\epsilon)) = \exp(\log p_{\hat{\phi}}(Y_i \mid \mathcal{T}_{\hat{\phi}}(\epsilon))),$$

$$\nabla_\phi p_{\hat{\phi}}(Y_i \mid \mathcal{T}_{\hat{\phi}}(\epsilon)) = \nabla_\phi \log p_{\hat{\phi}}(Y_i \mid \mathcal{T}_{\hat{\phi}}(\epsilon)) \cdot p_{\hat{\phi}}(Y_i \mid \mathcal{T}_{\hat{\phi}}(\epsilon)),$$

$$\nabla_{\phi}^2 p_{\hat{\phi}}(Y_i \mid \mathcal{T}_{\hat{\phi}}(\epsilon)) = \left(\nabla_{\phi}^2 \log p_{\hat{\phi}}(Y_i \mid \mathcal{T}_{\hat{\phi}}(\epsilon)) + \nabla_{\phi} \log p_{\hat{\phi}}(Y_i \mid \mathcal{T}_{\hat{\phi}}(\epsilon)) \nabla_{\phi} \log p_{\hat{\phi}}(Y_i \mid \mathcal{T}_{\hat{\phi}}(\epsilon))^{\top} \right) \cdot p_{\hat{\phi}}(Y_i \mid \mathcal{T}_{\hat{\phi}}(\epsilon)).$$

Finally, the Hessian of the log-marginal likelihood is computed as:

$$\nabla_{\phi}^2 \log p_{\hat{\phi}}(Y_i) = \frac{\nabla_{\phi}^2 p_{\hat{\phi}}(Y_i) \cdot p_{\hat{\phi}}(Y_i) - \nabla_{\phi} p_{\hat{\phi}}(Y_i) \nabla_{\phi} p_{\hat{\phi}}(Y_i)^{\top}}{p_{\hat{\phi}}(Y_i)^2}. \quad (7)$$

3 Solving the ODE of antibody kinetic and Identifiability Implications

We consider the following linear system of ODEs modeling antibody dynamics:

$$\begin{cases} \dot{S}(t) = \bar{f}_M(t) e^{-\delta_V(t-t_k)} - \delta_S(t) \\ \dot{Ab}(t) = \vartheta S(t) - \delta_{Ab} Ab(t) \\ (S(0), Ab(0)) = (0.01, 0.1) \end{cases}$$

Step 1: Solving the equation for $S(t)$ The ODE for $S(t)$ is linear and non-homogeneous.

We use the integrating factor method.

Integrating factor:

$$\mu(t) = e^{\delta_S t}$$

Multiply both sides:

$$e^{\delta_S t} \dot{S}(t) + \delta_S e^{\delta_S t} S(t) = e^{\delta_S t} \bar{f}_M(t) e^{-\delta_V(t-t_k)} \Rightarrow \frac{d}{dt} (e^{\delta_S t} S(t)) = e^{\delta_S t} \bar{f}_M(t) e^{-\delta_V(t-t_k)}$$

Integrate both sides:

$$e^{\delta_S t} S(t) = \int_0^t \bar{f}_M(\tau) e^{-\delta_V(\tau-t_k)} e^{\delta_S \tau} d\tau \Rightarrow S(t) = \int_0^t \bar{f}_M(\tau) e^{-\delta_V(\tau-t_k)} e^{-\delta_S(t-\tau)} d\tau$$

Final result:

$$S(t) = \left(\bar{f}_M(\cdot) e^{-\delta_V(\cdot-t_k)} \right) * e^{-\delta_S t}$$

This is a convolution of the input stimulus with an exponential decay kernel governed by δ_S .

Step 2: Solving the equation for $Ab(t)$ The equation for $Ab(t)$ is also linear:

$$\dot{Ab}(t) = \vartheta S(t) - \delta_{Ab} Ab(t) \Rightarrow Ab(t) = \int_0^t \vartheta S(\tau) e^{-\delta_{Ab}(t-\tau)} d\tau = \vartheta \cdot (S * e^{-\delta_{Ab}t})$$

Substitute the expression for $S(t)$:

$$Ab(t) = \vartheta \cdot \left(\left(\bar{f}_M(\cdot) e^{-\delta_V(\cdot-t_k)} \right) * e^{-\delta_S t} * e^{-\delta_{Ab} t} \right)$$

By associativity of convolution:

$$Ab(t) = \vartheta \cdot \left(\bar{f}_M(t) e^{-\delta_V(t-t_k)} * h(t) \right), \quad \text{where } h(t) = e^{-\delta_S t} * e^{-\delta_{Ab} t}$$

Interpretation: Convolution-Like Structure and Parameter Symmetry

The function $Ab(t)$ is obtained by a chain of linear filters (convolutions). First, the exogenous input $f_M(t) e^{-\delta_V(t-t_k)}$ is smoothed by the decay of $S(t)$ via convolution with $e^{-\delta_S t}$. Then, the antibody dynamics further smooth the result via convolution with $e^{-\delta_{Ab} t}$.

Because convolution of exponentials is commutative:

$$e^{-\delta_S t} * e^{-\delta_{Ab} t} = e^{-\delta_{Ab} t} * e^{-\delta_S t}$$

The final result $Ab(t)$ depends on the combined smoothing effect of δ_S and δ_{Ab} , not their individual identities. This leads to a key structural symmetry:

$$(\delta_S, \delta_{Ab}) \quad \text{and} \quad (\delta_{Ab}, \delta_S)$$

can yield the same $Ab(t)$ trajectory. Thus, the parameters δ_S and δ_{Ab} are Not structurally identifiable from $Ab(t)$ alone.

4 Optimization and Regularization

To improve convergence and generalization in sparse data regimes, we include the option dropout in the encoder network to prevent overfitting. To train the model, we maximize the

ELBO using stochastic gradient-based optimization. The Adam optimizer is used, and all gradients are computed using automatic differentiation with the software `Optax`. Optionally, we can use a cosine annealing learning rate schedule to facilitate smoother optimization.

In the simulation studies, model fitting is performed on a training dataset, while an independent validation dataset is generated from the same data-generating mechanism and used to monitor performance and tune hyperparameters. In the real-data application, where only a single dataset is available, we instead construct a validation set by splitting the observed data.

To ensure numerical stability and avoid premature stopping, we monitor three complementary convergence criteria during training: the gradient norm, the parameter update magnitude, and the validation loss evolution. Let s denote the epoch of the optimization algorithm.

Gradient norm criterion. Convergence toward a stationary point of the ELBO objective is assessed by the Euclidean norm of its gradient with respect to all model parameters (ϕ, ψ) :

$$\left\| \nabla_{(\phi, \psi)} \mathcal{L}_{\text{ELBO}}^{(s)}(\phi, \psi) \right\|_2 = \sqrt{\left(\sum_{j=1}^{D_\phi + D_\psi} \left(\frac{\partial \mathcal{L}_{\text{ELBO}}^{(s)}(\phi, \psi)}{\partial (\phi, \psi)_j} \right)^2 \right)} < \varepsilon_g,$$

where $\|\cdot\|_2$ denotes the Euclidean norm and ε_g is a small positive tolerance, typically in the range 10^{-5} – 10^{-3} . This condition indicates that further optimization steps would lead to negligible improvement in the objective.

Parameter update criterion. Convergence in parameter space is additionally checked by comparing successive parameter estimates:

$$\frac{\left\| (\phi, \psi)^{(s)} - (\phi, \psi)^{(s-1)} \right\|_2}{\left\| (\phi, \psi)^{(s-1)} \right\|_2 + \varepsilon} < \varepsilon_p,$$

$$\left\| (\phi, \psi)^{(s)} - (\phi, \psi)^{(s-1)} \right\|_2 = \sqrt{\left(\sum_{j=1}^{D_\phi+D_\psi} \left((\phi, \psi)_j^{(s)} - (\phi, \psi)_j^{(s-1)} \right)^2 \right)},$$

and ε_p is a small threshold (typically 10^{-7} – 10^{-5}) and ε (typically 10^{-8}) prevents division by zero. This criterion ensures that the parameter updates have become sufficiently small.

Validation loss criterion. Finally, an early stopping rule is applied based on the validation ELBO loss $\mathcal{L}_{\text{val}}^{(s)}$:

$$\mathcal{L}_{\text{val}}^{(s)} > \min_{s' < s} \mathcal{L}_{\text{val}}^{(s')} \quad \text{for more than } P \text{ consecutive epochs,}$$

where P is a predefined patience parameter. This prevents overfitting by stopping training once the validation performance no longer improves.

5 Simulation details

To ensure positivity of the variance parameters, the encoder outputs log-standard-deviation, i.e. it predicts $\log(\Sigma_\psi(Y_i))$, and we estimate $\log(\Sigma^2)$ for the observation noise.

All experiments were run on a single machine equipped with an NVIDIA A100 GPU (40 GB), using float64 precision. Importantly, the proposed VAE-based NLME-ODE approach is not GPU-intensive: we were able to run the full pipeline on a standard laptop (Intel Core i7 CPU with an NVIDIA RTX 2000 GPU) including the variance estimation step, though it is slower than on the A100. The pipeline can also be run on CPU-only hardware with the same workflow and is slower still.

For the SAEM benchmark, we used `Monolix 2023R1` on a high-performance CPU server equipped with 2x 16-core Skylake Intel Xeon Gold 6142 @ 2.6 GHz and 384 GB of RAM. For most models, Monolix was run with default settings, which include using `autoChains = TRUE`, meaning Monolix automatically determines the number of MCMC chains (starting

from one) based on internal convergence diagnostics. The simulated annealing option is enabled which permits to keep the explored parameter space large for a longer time. For the complex settings in the antibody kinetic model and the TGF- β model, we used a more robust configuration to stabilize SAEM convergence. In particular, we set the number of chains as 10 and customized the MCMC strategy to $c(5, 2, 5)$, giving more iterations to the blockwise kernel, which improves mixing in these models. We also increased the burn-in period to 100 iterations and used default 500 exploratory iterations with auto-stop disabled. Finally, we set the smoothing interval to 300 and disabled automatic smoothing, which avoids premature variance shrinkage.

5.1 Pharmacokinetic model

In this simulation, the true population parameters are: In the irregular sampling setting, we

Parameter	Description	True value
ϑ_1	Elimination rate of $X_{1,i}$ (individual-specific)	0.5
ϑ_2	Transfer rate from $X_{2,i}$ to $X_{1,i}$	2
ω_{ϑ_1}	Std. dev. of random effect on ϑ_1	0.5
σ_ε	Residual error standard deviation	0.2

Table 1: True parameter values used in the simulation datasets of the pharmacokinetic model

used a single-layer Gated Recurrent Unit (GRU) with hidden state of dimension 16 in the encoder. The final GRU hidden state is mapped through a linear layer to a 4-dimensional embedding, followed by a GELU nonlinearity.

In addition, we used a custom initialization for the final linear layer: weights were re-initialized from a normal distribution with a small standard deviation (0.001) to prevent

excessively large activations and variance at the beginning of training. We used an initial learning rate of 0.1. If the monitored metric did not improve for 50 consecutive epochs, the learning rate was reduced to 0.05. Training was stopped if no improvement was observed for 100 epochs. We integrated the ODEs using the adaptive fifth-order explicit Runge–Kutta method (Dormand–Prince 5(4);`dopri5`) with `rtol = atol = 10-8`. The average training time was approximately 20 minutes.

5.2 Antibody kinetics

For the implementation of the encoder, in the regular sampling design we applied `Conv1d` with `kernel_size=3` and a latent representation of dimension 4. For the irregular sampling design, we replaced the convolutional feature extractor with a single-layer GRU with hidden dimension 32 to encode the input sequence. We used an initial learning rate of 0.05. If the monitored metric did not improve for 200 consecutive epochs, the learning rate was reduced to 0.01. The same solver is used as in 5.1. Training was stopped if no improvement was observed for 500 epochs. The average training time was approximately 45 minutes.

5.3 TGF- β dynamics

The parameter values were chosen as shown in table 3. In this simulation, we used the same encoder architecture as in the antibody kinetic model for the regular sampling, but with a larger convolutional receptive field by setting `kernel_size=7`. The L-stable fifth-order ESDIRK method `Kvaerno5` with `rtol = atol = 10-6` is used to integrate the ODEs. Optimization was performed with a default learning rate of 5×10^{-4} , and we applied global gradient clipping using `optax.clip_by_global_norm(1.0)` to improve numerical stability during training. The underlying dynamic system is moderately stiff with strongly coupled states, which can lead to ill-conditioned optimization and occasional large gradient

Parameter	Description	True value
ϑ	Antibody production rate	24.5
\bar{f}_{M_2}	Memory factor after 2nd injection	7.1
\bar{f}_{M_3}	Memory factor after 3rd injection	18.5
δ_S	Secreting cell decay rate	0.01
δ_{Ab}	Antibody degradation rate	0.08
ω_ϑ	Std. dev. of random effect on ϑ	0.5
$\omega_{\bar{f}_{M_2}}$	Std. dev. of random effect on \bar{f}_{M_2}	0.9
t_0	First injection time (Days)	0
t_1	Second injection time (Days)	30
t_2	Third injection time (Days)	250
ϵ_{Ab}	Residual error standard deviation	0.1

Table 2: True parameter values used in the simulation datasets of antibody kinetic model

norms (e.g., due to sensitivity amplification through the ODE solver). Clipping the global gradient norm prevents severe exploding updates and helps maintain steady progress in ELBO optimization. Due to the computational cost of integrating the stiff ODE system, the average training time was approximately 70 minutes.

5.4 Real-world antibody kinetic dataset

In real-world applications, longitudinal sequences typically have variable lengths. To enable efficient batching, we pad each sequence to a common length T (the maximum sequence length in the dataset) and define a binary mask $m_{it} \in \{0, 1\}$ indicating whether time step t for subject i is observed ($m_{it} = 1$) or corresponds to padding/missingness ($m_{it} = 0$). The mask is applied throughout the encoder and in the reconstruction term, ensuring that padded

Parameter	Meaning	Value
k_p	Proliferation rate of ASM	1.15
ω_{kp}	Std. dev. of random effect on k_p	0.05
k_{ac}	Activation rate of TGF- β via ASM contraction	0.01
k_b	TGF- β binding rate to ASM receptors	1.00
ϕ_c	Contractile ASM apoptosis rate	0.10
k_s	Amplitude of external stimulus	0.20
ν	Stimulus duration	30.0
τ_i	Stimulus times	[50, 90, 130, 170, 210]
ϵ_a	Residual error standard deviation	0.1

Table 3: Parameter values used in the TGF- β model simulations (diseased-state regime).

Parameters not listed here were fixed to their baseline values reported in Table A4 of

positions neither affect the pooled representation nor contribute to the objective. We then use masked attention pooling to aggregate variable-length sequences. Let $z_i = (z_1, \dots, z_T)$ be a sequence of hidden states per subject with the vector $z_t \in \mathbb{R}^H$ after the convolution layer where H is the dimension of the hidden state. We compute a scalar attention logit for each time step using a learned linear map:

$$e_t = w^\top z_t + c, \quad w \in \mathbb{R}^H, c \in \mathbb{R}.$$

Masking is enforced by assigning a large negative value to invalid positions:

$$\tilde{e}_t = \begin{cases} e_t, & \text{if } m_t > 0, \\ -10^9, & \text{otherwise.} \end{cases}$$

The attention weights are then obtained by a softmax over time step,

$$\alpha_t = \frac{\exp(\tilde{e}_t)}{\sum_{t=1}^T \exp(\tilde{e}_t)}, \quad t = 1, \dots, T,$$

so that $\sum_{t=1}^T \alpha_t = 1$ and masked positions receive numerically zero weight. Finally, the pooled representation is a combination of the hidden states:

$$\text{pool}(z, m) = \sum_{t=1}^T \alpha_t e_t \in \mathbb{R}^H.$$

This pooling layer produces a H -dimensional summary vector while allowing the model to focus on the most informative time steps and ignore padded/missing entries through the mask.

We padded each subject trajectory to a common length 17 with a binary mask and applied a `Conv1d` with `kernel_size=1` and `output_channels = 16`. The resulting padded sequence is summarized via masked attention pooling and then the pooled vector of \mathbb{R}^{16} was transformed as an embedding of 4-dimension.

In the training, with only 25 subjects available, splitting the data into separate training and validation sets would leave too few subjects in the validation subset, leading to extremely noisy validation metrics and unstable hyperparameter selection. We therefore used all available subjects for training and tune hyperparameters based on convergence assessment and overfitting diagnostics, by monitoring ELBO trajectories, stability of the estimated population parameters, and posterior predictive fit. The average training time was approximately 20 minutes.